Modeling and Optimal Design of a Desalination System Integrated Between a Glass-Covered Solar Collection Water Chamber and a Heat Dissipating Chimney

Qichao Hu
Department of Aerospace and Mechanical Engineering,
University of Arizona,
Tucson, AZ 85721
e-mail: huqichao@arizona.edu

Peiwen Li[1]
Department of Aerospace and Mechanical Engineering,
University of Arizona,
Tucson, AZ 85721
e-mail: peiwen@arizona.edu

Solar thermal energy is trapped in a glass-covered water chamber/basin to provide the heat for evaporation of brackish water in a novel desalination system. To harvest clean water, a chimney is integrated with the water basin, which draws air into the chamber to be humidified by the vapor and then being ventilated via buoyance force. Uniquely, thermal conductive metal sheet is recommended to make the chimney, which allows the vapor in the humid air condenses easily when flowing up. The condensate at the inner wall of the chimney flows down to be collected as clean water. Mathematical modeling and numerical computation have been carried out to delineate the coupling of the buoyance-force-driven flow with the heat and mass transfer of air and water in the solar collection chamber and the condensation of vapor in the heat-dissipating chimney. The objective of the simulation and optimization of the system is to find the best match of the dimensions of the water chamber with a chimney to maximize the production of clean water and energy efficiency. The model has been used to simulation several cases (of water from 40 °C to 50 °C) with available experimental data from the authors' previous work, and the agreement was satisfactory. The optimization studies found that there is a maximum air flowrate corresponding to a critical chimney height due to the requirement that the chimney is designated to dissipate heat as much as possible to condense water vapor. With the chimney height greater than the critical height, the airflow rate will have a slight decrease. Nevertheless, higher than a critical height is still needed for a chimney to condense more moisture. Optimized chamber diameters at different chimney heights are provided for reference of optimal system designs.
[DOI: 10.1115/1.4056879]

Keywords: words: solar desalination, heat-dissipating chimney, modeling and simulation, optimization, critical chimney height, energy systems, heat and mass transfer, thermal systems

1 Introduction

Clean water is essential and critical to the sustainable development and prosperity of human society in the future, because human beings, animals, and the growth of plants need clean water with a salinity level below 1000 ppm. Although the earth has a huge amount of water, the salinity level of a significant part of natural water sources on the earth is above 10,000 ppm, and seawater even has a salinity of 35,000–45,000 ppm [1]. Therefore, to obtain low salinity clean water, desalination becomes the primary approach, which is more and more relied on for solving the water shortage problems around the world [2].

Desalination processes require a significant amount of energy. Most traditional desalination systems use either electrical energy or thermal energy that comes from the combustion of fossil fuels, which is believed to cause air pollution, global warming [3], and even water pollution. In recent years, renewable energy technology has progressed significantly; therefore, using renewable energy, particularly solar energy, for desalination has become one of the most clean and low-carbon-emission water technologies. Li et al. [4] and Alkaisi et al. [5] advocate that solar energy be used for desalination because solar energy can be converted into either thermal or electrical energy, which can be used in different desalination technologies.

Zhang et al. [6] recommended that mainstream desalination technologies be classified into three categories. These are (1) distillation using thermal energy through evaporation and condensation processes; (2) direct separation of water and salts using reverse osmosis (RO) membranes that needs mechanical work to build up a great pressure difference across the membrane; and (3) using an electrical field to drive the separation and exclusion of positive and negative ions of salts from water. Comprehensive reviews of thermal distillation desalination are available in the literature [7–9]. Specific technologies of this category include humidification–dehumidification (HDH), multi-effect distillation (MED) [10,11], multi-stage flash (MSF) [12], and membrane distillation (MD) [13,14]. Reverse osmosis desalination systems need to use pumps to build up very large pressure differences across a membrane to separate water and salts [15]. Developing high-performance and endurance membranes dominates the research interest for RO desalination [16,17]. Electrodialysis (ED) desalination relies on an electrical field to separate and remove ions in a salt solution [18]. The thermal energy or electrical energy for these desalination technologies may come from solar energy which can be converted to either thermal energy or electrical energy as needed. Depending on whether the solar collection system is separated from the desalination system, there are solar-driven direct and indirect desalination systems. From the perspectives of system

[1]Corresponding author.

Manuscript received September 13, 2022; final manuscript received January 29, 2023; published online March 31, 2023. Assoc. Editor: Rui Qiao.

capital cost and expenses on maintenance of operation, direct solar thermal desalination is more attractive because of the system's compactness and less demand for maintenance.

Solar stills are typical direct solar desalination systems that have one chamber to accomplish functions of solar collection, water evaporation, and vapor condensation for the collection of distilled water [19,20]. A solar still is a closed system [21], where a limited amount of air enclosed inside the chamber is humidified at a high temperature, and at the low-temperature glass surface, moisture is condensed as clean water. The cover glass typically does not have very high thermal conductivity, which is not favorable to heat release and vapor condensation, and the condensed water film or drops at the glass surface may reflect and reduce the sunlight from entering the chamber. Although possessing the advantage of simplicity and compact structure, traditional solar stills are mostly suitable for small-scale desalination, and the energy efficiency is approaching 30% so far [22]. To overcome the problems of enclosed solar stills, an open system has been proposed to drive the fully humidified air to flow from the solar still into a cooling system, which is the so-called active solar stills [23]. The active solar still reported in the literature by Tiwari et al. [24] has solar still coupled with a flat plate thermal collector. Sampathkumar et al. [25] also reported pre-heated water solar still with the addition of a thermal storage function for extended operation at night. It is understood that the active solar stills have been found promising for higher efficiency due to the active flow of air in the system [24].

In order to introduce active air flow for solar stills, there have been some efforts of making use of a solar chimney power generation system to provide active airflow for desalination. A solar chimney power system is typically a very large device that allows ambient air entering the solar collection chamber to be warmed up, and the chimney ventilates the air [26,27]. The airflow passes through a power generation turbine at the entrance of the chimney to generate electrical power. Zuo et al. [28–30] tried to install a solar still inside the solar collection chamber of a solar chimney power generation system. They also designed another system which has a water pond inside the solar collector, and a condenser below the turbine was installed to capture more water condensate [31]. Following the work of Zuo et al. [28], Zhou et al. [32] installed a condenser at the top of the solar chimney to increase the condensation of water vapor. Using the numerical computational method, Asayesh et al. [33] studied a solar collection chamber, which has a diameter of 250 m and a chimney of 200 m high, and a shallow water pond covers the bottom of the chamber from the outer edge to the location of the diameter of 85 m. Ming et al. [34–36] also proposed to install a seawater sprayer below the turbine to humidify the air before it enters the chimney.

It is important to point out that in a regular solar chimney power generation system or in the systems mentioned in the above paragraph, the chimney has been always set as adiabatic to maximize the airflow through the system and thus produce electrical power [37–39]. However, an adiabatic chimney does not allow heat dissipation and thus is not helpful for the process of desalination. To bridge the research gap, the current authors propose to focus on desalination application without installing the turbine in the system, and more importantly, a thin metal-sheet chimney is uniquely used so that the heat dissipating from the chimney will help the condensation of the vapor and thus more water can be collected. If the system is solely designed for desalination, the required dimensions of the system could be significantly flexible and do not have to be very huge. With these new considerations, a solar collection chamber is modified entirely as a water basin/chamber for both solar collection and water evaporation. Heat transfer enhancement both in and outside of the chimney can be applied. A reflective coating at the exterior of the metal-sheet chimney may also be applied to reflect sunlight and increase cooling to the chimney [40]. Such a chimney system is completely different compared to the adiabatic chimney used for solar chimney power systems. The proposed concept was first proven by the authors in a test from June to August of 2018 in Tucson, AZ, USA [41]. The water temperature in this test reached 60 °C, and clean water was collected in the chimney. The outdoor experiment was subjected to variations in sunlight and ambient temperatures. Therefore, to investigate the effect of every parameter on the desalination performance, in-lab experiments with controlled heating and water temperatures were conducted and reported by the authors in 2020 [42].

It needs to point out that the airflow entering the system and the water evaporation and condensation are determined by highly coupled factors including the dimensions of the solar collecting water basin, the height of the heat-dissipating chimney, and the temperatures of the water and ambient air. To clearly understand the effect of these parameters on the desalination performance, a mathematical model and computation are very necessary, which is the focus of this paper. The model will be used to investigate and optimize the designs of the water desalination system. As the final goal, the computation code will provide a tool for engineering design and applications.

2 Physical Details of the Novel Solar Thermal Desalination System

Figure 1 illustrates the novel desalination system. A water basin, also serving as the solar collection chamber, and a heat-dissipating chimney are integrated to accomplish the goal of distillation for making clean water. The solar collection chamber is covered by transparent glass with its low thermal conductivity as a favorable property. The basin may have a black floor and black blocks to absorb sunlight entering the chamber. Sunlight converts to thermal energy and is mostly trapped due to the greenhouse effect. Solar thermal energy can warm up the water in the basin to temperatures above the ambient air temperature. Dry air from outside of the system can enter the water basin, being warmed and humidified by the vapor from the water surface. With the density of the humid and warm air being smaller than that of the ambient air, the buoyance force will drive the humid air to flow up in the chimney and be ventilated. Since the buoyance-force-driven flow of air occurs naturally, dry air keeps entering the system and takes water vapor to the heat-dissipating chimney. If there is sufficient cooling to the chimney, water vapor will condense inside the chimney. This is the reason that the chimney must be made of thin metal sheet which can dissipate heat from the warm humid air to the lower temperature ambient air outside of the chimney.

Several important observations to the physics of the solar desalination system are noted for the effective production of clean water. First, drawing sufficient airflow to the system via buoyance force in the chimney is important because more airflow can uptake more

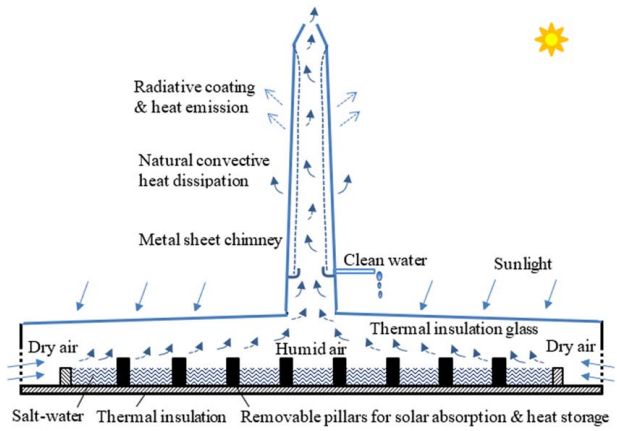

Fig. 1 Concept of glass-covered solar collection water basin integrated with a heat-dissipating chimney for condensation of water vapor into clean water

water vapor. Second, dry air is better to be fully humidified to a relative humidity of 1.0 before it enters the chimney so that vapor condensation can occur from the bottom of the chimney. To meet the first condition, a sufficiently large area of water basin must be available, so that the mass transfer of vapor from the water surface to the air can meet the requirement of relative humidity of 1.0 for the airflow. Third, the heat dissipation from the chimney must be sufficient to cool humid air as much as possible for condensation. Enhanced heat transfer inside and outside of the heat-dissipating chimney, as well as the large temperature difference between the hot (or warm) humid air in the chamber and the ambient air, can all contribute to heat dissipation.

Designing a system that can satisfy the above requirements is challenging if only relying on experimental studies. Therefore, mathematical analysis is very necessary for a better understanding of the correlations between the dimensions of chimney and the water basin, the airflow rate drawn to the system, and the effect of the temperatures of water and ambient air on the water production rate. Section 3 in the following will discuss the mathematical modeling and algorithm of computations for the analysis and design of such a system.

3 Mathematical Modeling of Multi-Physics in the System

The goal of mathematical modeling of the proposed solar desalination system is to provide a design tool to determine the diameter of the water chamber with given conditions including the height and diameter of the chimney, the temperatures of the water and ambient air, and the space between the water surface and the cover glass. One important condition that dictates the determination of the diameter of the water chamber is that the dry air entering the system must be fully humidified to a relative humidity of 1.0 in the water chamber before entering the heat-dissipating chimney. Another critical condition is that the energy usage per unit area at the water surface is restricted to 60% of the solar energy density of 1000 W/m^2 per the report in literature that greenhouses may take 60% of solar energy [35].

Obviously, the flow is driven naturally by the buoyance force. The first and foremost parameter that needs to be determined is the flowrate of air. However, the buoyance force in the system is related to the density of humid air, which is determined by the humidity and temperature of the humid air. Therefore, the determination of the air flowrate and the evaporation and condensation-related heat and mass transfer is coupled/interrelated. Solving the relevant equations in a coupled manner with a proper algorithm will allow us to get converged results about air flowrate, water evaporation rate, as well as condensation rate of the vapor. The following four aspects of mathematical modeling are considered to accomplish the goal of finding the converged solutions:

(1) The mass flowrate of air entering the system is caused by natural convection. A mass flowrate of the airflow is decided so that the pressure loss of the airflow in the system equals the driving force that introduces the flow. The driving force causing the airflow is determined from the buoyance force of warm and humid air flowing in the heat-dissipating chimney. However, the density of humid air is a function of the humidity and temperature of the air which must be determined by the heat and mass transfer in the following steps.

(2) The humidity of the air flowing inside the chamber is determined by the mass transfer of vapor from the evaporative water surface to the air stream. For choosing a proper water chamber diameter, it needs to check if the dry airflow can be fully humidified in the water basin, if not, the area of the water basin will be increased, and computations will have to start again from *step (1)*. It is noted that the mass transfer computation needs the flowrate and the temperature of the air, which needs analysis in *steps (1)* and *(3)*.

(3) Based on the preset temperature of water in the basin, heat transfer and total energy balance analysis is needed to find out the temperatures of humid air in the water basin and the heat-dissipating chimney. From the energy balance point of view, the energy spent for the evaporation and the heat goes from the water surface to the airflow should equal the solar energy that is projected to be obtained in the water basin. To meet the projected energy usage or heat flux in the water chamber, the water surface temperature in the basin can be adjusted, or the water basin area can be re-adjusted to obtain a different air flowrate, which needs new computations from *step (1)*.

(4) With the air flowrate and temperatures determined in *steps (1)–(3)*, the temperature and condensation rate of water vapor inside the heat-dissipating chimney can be decided through the heat transfer analysis for the convective flow inside chimney and natural convection outside of the chimney. The temperature of the humid air in the chimney will feedback to determine the driving force of the airflow in the entire system.

It is important to point out that iterative computation is needed. This means that after *step (4)*, the obtained temperatures and humidity of air should be used in *step (1)* again to obtain an updated flowrate in a new iteration from *steps (1)* to *(4)* until every parameter is converged.

Sections 3.1–3.5 describes the computational domain for the analysis and the equations for the determination of the air flowrate and the heat and mass transfer.

3.1 Computational Domain and Discretization. Figure 2 shows the computational domain. The mathematical modeling of flow, heat, and mass transfer will be conducted with respect to the space that airflow passes from the edge (the inlet) of the chamber to the exit of the chimney. We consider the heat-dissipating chimney as a pipe with high thermal conductivity.

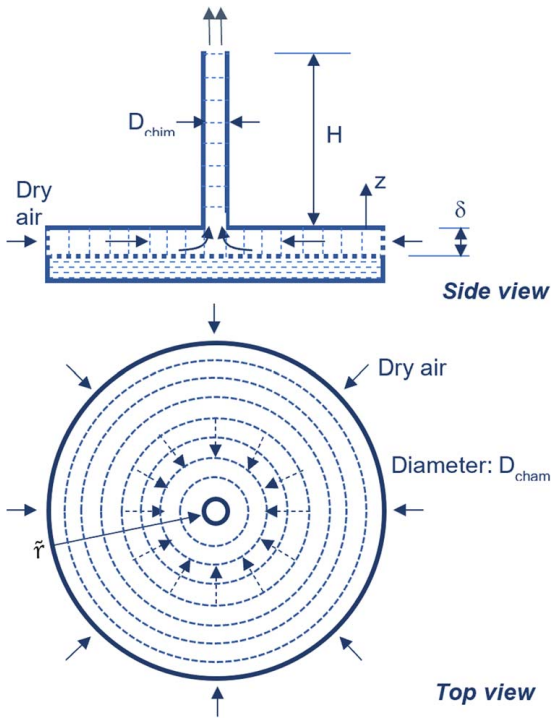

Fig. 2 The side and top views of the system and mesh for control volumes

The water temperature is assumed to be known and constant but will be checked and updated based on the energy balance. The calculated energy in water evaporation is viewed as the solar energy that is absorbed in the chamber. As the water temperature is assumed in the computation, the amount of solar energy absorbed in the solar collection chamber is an indirectly given condition. If this calculated energy has a reasonable range (100–1000 W/m^2), the assumption of the water temperature is considered reasonable. The ambient air is assumed static with known temperature.

The discretization of control volumes was applied to the humid airflow in the chimney, as well as the space above the water surface in the water basin. The control volumes are cylindrical in the chimney and annulus in the chamber as indicated by the dashed lines and circles in Fig. 2. The dimension of a control volume in the flow direction was decided as 0.01 m based on mesh-independent study. The calculations for flow and heat/mass transfer in control volumes march forward along the flow direction of air from the edge/inlet of the water basin to the exit of the chimney.

3.2 Mass Flowrate of Air From the Balance of Buoyancy Force and the Pressure Loss of the Flow in the System. The driving force that introduces the airflow to the system comes from the fact that the density of warm and humid air inside the chimney is less than that of the ambient air outside of the chimney. Therefore, due to the buoyancy force, the warm and humid air rises inside the heat-dissipating chimney, which drives the overall flow in the entire desalination system. The amount of air that enters the system is determined when the driving force and the friction loss of flow in the entire system are balanced. The following equation expresses the driving force for the flow in the desalination system [43]

$$\Delta P_{drive} = \int_0^H g(\rho_{out\_dryair}(z) - \rho_{in\_moistair}(z))dz \tag{1}$$

where $\rho_{out\_dryair}(z)$ is the density of dry air outside of the chimney, which changes slightly with the altitude, z, in the form of [44]

$$\rho_{out\_dryair}(z) = \rho_{atm} * \left(1 - \frac{\kappa - 1}{\kappa}\frac{z}{H_0}\right)^{1/(\kappa-1)} \tag{2}$$

where ρ_{atm} is the air density based on ground level and local temperature; κ is 1.235, and the atmospheric height is given as $H_0 = R_{air}T_{air}/g$.

The pressure loss from the converging flow in the water basin and in the heat-dissipating chimney should be overcome by the driving force (expressed in Eq. (1)). The pressure drop in the airflow path includes the major loss and minor loss added together. The major loss is the friction loss in the solar collection chamber and in the heat-dissipating chimney, which can be determined by the Darcy–Weisbach equation [45]

$$\Delta P_{friction} = \int \frac{1}{2}\frac{f * \rho * u^2}{D_h} dx \tag{3}$$

where dx represents the size of one mesh in the radial direction of the water basin and the height of the chimney, and D_h is the hydraulic diameter of the flow channel. The Moody friction factor is f, which can be calculated with the following equations for laminar flow and turbulent flow [45]

$$f = \begin{cases} \frac{64}{\mathrm{Re}} \text{ (for chimney)}, \quad \frac{96}{\mathrm{Re}} \text{ (for chamber)} & \mathrm{Re} < 2300 \\ (0.790 \times \ln(\mathrm{Re}) - 1.64)^{-2} & \mathrm{Re} > 2300 \end{cases} \tag{4}$$

It needs to point out that the cross-sectional flow area and the perimeter of airflow in the water basin vary with the diameter of the control volume. Therefore, the hydraulic diameter, D_h, of the flow in a control volume in the water chamber is determined as [45]

$$D_h = D_{cham}^{cross} = \frac{4\pi r_{cham}\delta}{2\pi r_{cham} + \delta} \tag{5}$$

Because the airflow velocity and the hydraulic diameter in the water chamber vary along the flow, the Reynolds number in Eq. (4) also varies along the flow.

The minor pressure loss due to the change of the flow channel from the water basin to the chimney is given as

$$\Delta P_{minor} = \frac{K u_{average}^2}{2g} \tag{6}$$

where K is the minor loss coefficient. For a 90-deg bent of flow channel, K is 0.3 [46]. The average velocity $u_{average}$ is the velocity when the flow goes from the water basin to the chimney inlet.

In the earlier analysis, the local densities, $\rho_{in\_moistair}(z)$, for the moist air in the chimney, and ρ in the water chamber, are functions of the humidity and temperature, which need to be determined from the heat transfer and mass transfer analyses in Secs. 3.3–3.5.

3.3 Heat Transfer in the Solar Collecting Water Basin. The objective of the analysis of the heat transfer between the airflow and the water in the solar collection chamber is to decide the streamwise local temperatures of the air and the heat loss to ambient air at a given water temperature of the basin. Figure 3 shows a control volume (by dashed lines) which is a cross section of one of the annuluses indicated in Fig. 2 in the radial direction of the water basin.

The energy conservation equation at a steady-state condition in a control volume is given as

$$\begin{aligned} 0 = {} & \dot{Q}_{CB} + \dot{m}_{air}(\tilde{h}_{air-in} + x_{cham-in}\tilde{h}_{g-w-in}) \\ & - \dot{m}_{air}(\tilde{h}_{air-out} + x_{cham-out}\tilde{h}_{g-w-out}) + \dot{m}_{w-ev}\tilde{h}_{g-w-ev} \end{aligned} \tag{7}$$

where $\tilde{h}_{g-w}$ is the enthalpy of water vapor. The enthalpy of air is $\tilde{h}_{air} = Cp_{air}T$, where Cp_{air} is the heat capacity of air. The heat transfer across the boundary, $\dot{Q}_{CB}$, includes the part from water surface to airflow $\dot{Q}_{w-a}$, and the heat loss across the glass cover $\dot{Q}_{loss}^{cham}$, which gives

$$\begin{aligned} \dot{Q}_{CB} = {} & \dot{Q}_{w-a} - \dot{Q}_{loss}^{cham} = A_{cham}^{surface} * h_{cham} * (T_{water} - T_{a-cham}) \\ & - U_{cham} * (T_{a-cham} - T_{air}) \end{aligned} \tag{8}$$

where T_{a-cham} is the average airflow temperature at the inlet and outlet of a control volume. $A_{cham}^{surface}$ is the heat transfer surface area between water and airflow in the chamber for a control volume. The overall heat transfer coefficient U_{cham} (W/m^2-K) is calculated in the form of

$$U_{cham} = \frac{A_{cham}^{surface}}{\frac{1}{h_{cham}} + \frac{t_{glass}}{k_{glass}} + \frac{1}{h_{ncham}}} \tag{9}$$

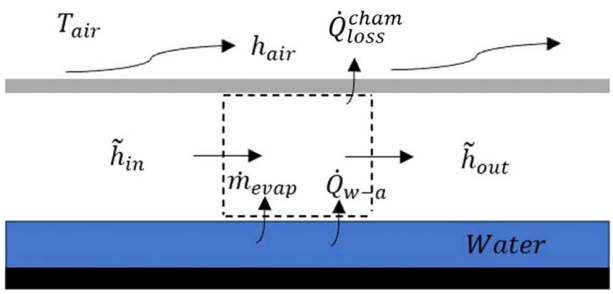

Fig. 3 Heat transfer of a control volume inside the solar collector chamber

where k_{glass} is the thermal conductivity of the glass material. The convection heat transfer coefficient of moist air inside the chamber is $h_{cham} = Nu_{cham} * k_{m-air}/D_{cham}^{cross}$ (W/m^2 − K), which is determined from the Nusselt number. The following expression gives the Nusselt number of the heat transfer inside the chamber for laminar and turbulent flows depending on the Reynolds number [46]

$$\mathrm{Nu}_{cham} = \begin{cases} 4.86 & \mathrm{Re}_{cham} < 2300 \\ \dfrac{\left(\frac{f}{8}\right)(\mathrm{Re}-1000)\mathrm{Pr}}{1+12.7\left(\frac{f}{8}\right)^{\frac{1}{2}}\left((\mathrm{Pr})^{\frac{2}{3}}-1\right)} & 2300 < \mathrm{Re}_{cham} \end{cases} \quad (10)$$

The natural convection heat transfer coefficient on the outer surface of the cover glass is $h_{n-cham} = Nu_{n-cham} \times k_{air}/D_h^{entire-surfcae}$ (W/m^2 − K), where the characteristic length $D_h^{entire-surfcae}$ is the rate of the entire surface area of the cover glass against the perimeter of the entire cover glass. The Nusselt number of natural convection on the outer surface of the glass is [47]

$$\mathrm{Nu}_{n-cham} = \begin{cases} 0.54(\mathrm{Gr}_{n-cham} \times \mathrm{Pr}_{n-cham})^{\frac{1}{4}} & 10^4 < \mathrm{Gr}_{n-cham}\mathrm{Pr}_{n-cham} < 10^7 \\ 0.15(\mathrm{Gr}_{n-cham} \times \mathrm{Pr}_{n-cham})^{\frac{1}{4}} & 10^7 < \mathrm{Gr}_{n-cham}\mathrm{Pr}_{n-cham} < 10^{11} \end{cases} \quad (11)$$

where Gr_{n-cham} is the Grashof number for natural convection.

The mass conservation equation with a steady-state condition in a control volume in the chamber is given as

$$0 = \dot{m}_{cham-in}^{total} + \dot{m}_{w-ev} - \dot{m}_{cham-out}^{total} \quad (12)$$

where $\dot{m}_{w-ev}$ represents the water evaporation rate in a control volume. The mass flowrate of air is constant. Therefore, the total flowrate is $\dot{m}_{cham}^{total} = \dot{m}_{cham}^{vapor} + \dot{m}_{air}$, and the mass flowrate of vapor at a control volume is given in the form of

$$\dot{m}_{cham-out}^{vapor} = \dot{m}_{cham-in}^{vapor} + \dot{m}_{w-ev} \quad (13)$$

Here, the water evaporation rate will be determined through mass transfer analysis in Sec. 3.4.

3.4 Airflow Mass Transfer in a Control Volume in the Solar Collection Water Chamber. The mass transfer of the vapor from the water surface to the air in the water basin needs to be solved in order to find out the humidity of the air in the chamber. From the amount of water vapor transferred in the air, we can calculate the humidity of the air. The humidity of the air is also monitored as an important condition for the determination of the size of the water chamber. Only when the air is fully humidified and flows to the heat-dissipating chimney, can it be sure that the maximal amount of water vapor will condense in the chimney.

Inside a control volume, the evaporation rate of water is due to the diffusion of water vapor to the airflow. Therefore, the mass transfer rate is the evaporation rate, $\dot{m}_{w-ev}$ (kg/s), which is expressed as

$$\dot{m}_{w-ev} = \begin{cases} A_{cham}^{surface} \times h_{m-cham}(\rho_{water-cham}^{vapor} - \rho_{a-cham}^{vapor}) & \mathrm{RH}_{cham} < 1 \\ 0 & \mathrm{RH}_{cham} = 1 \end{cases} \quad (14)$$

where the relative humidity is the partial pressure of water vapor in the humid air against saturated pressure of water at the temperature:

$$\mathrm{RH}_{cham} = \frac{P_{cham}^{vapor}}{P_{cham}^{sat-vapor}} \quad (15)$$

In Eq. (14), the mass concentration, $\rho_{water-cham}^{vapor}$, of water vapor at the water surface is determined using ideal gas law as a function of the saturated pressure of water vapor and the water temperature. If the absolute humidity of air is known, the water vapor concentration in the airflow in a control volume is easily calculated, as given in the Appendix.

The mass transfer coefficient is based on the mass diffusivity and the Sherwood number, $h_{m-cham} = D_{v-air} \times \mathrm{Sh}_{v-air}/D_{cham}^{cross}$ (m/s). The Sherwood number Sh_{v-air} of the mass transfer is a function of Reynolds number and Schmidt number Sc_{v-air}, which is determined from the following equations [46]:

$$\mathrm{Sh}_{cham} = \begin{cases} 4.86 & \mathrm{Re}_{cham} < 2300 \\ 0.023 \times (\mathrm{Re}_{cham})^{0.83}(\mathrm{Sc}_{v-air})^{0.33} & 2300 < \mathrm{Re}_{cham} \end{cases} \quad (16)$$

$$\mathrm{Sc}_{v-air} = \frac{\mu_{v-air}}{\rho_{v-air} \times D_{v-air}} \quad (17)$$

where the mass diffusivity is determined by Chapman–Enskog relationship [45]

$$D_{v-air} = \frac{(1.8583 * 10^{-7}) \times T_{w-a}^{\frac{3}{2}}}{P_{atm} \times \Omega_D^{va}} \sqrt{\frac{1}{M_{water}} + \frac{1}{M_{air}}} \quad (18)$$

The collision integral Ω_D^{va} is given as

$$\Omega_D^{va} = \sigma_{va}^2 \Omega_D(k_B T_{w-a}/\varepsilon_{AB}) \quad (19)$$

where T_{w-a} (K) is the average temperature of water surface and airflow, the collision diameter $\sigma_{va} = (\sigma_v + \sigma_a)/2$, $\sigma_v = 2.655$ (Å), and $\sigma_a = 3.711$ (Å), which represent the molar diameter of the collisions of water vapor and air. The collision integral Ω_D is determined [45] with known $\varepsilon_{AB} = \sqrt{\varepsilon_A \varepsilon_B}$, where $\varepsilon_A/k_B = 363$ (1/K) and $\varepsilon_B/k_B = 78.6$ (1/K)

3.5 Water Vapor Condensation Heat Transfer in the Heat-Dissipating Chimney. The heat transfer analysis for the humid airflow in the chimney is conducted to find out the amount of condensation of water vapor in the entire chimney. The energy conservation equation at a steady-state condition for the humid airflow in a control volume in the chimney, as shown in Fig. 4, is given by the following equation:

$$0 = -\dot{Q}_{loss} + \dot{m}_{air}(\tilde{h}_{air-in} + x_{chim-in}\tilde{h}_{g-w-in}) - \dot{m}_{air}(\tilde{h}_{air-in} + x_{chim-out}\tilde{h}_{g-w-out}) - \dot{m}_{w-cd}\tilde{h}_{f-w-cd} \quad (20)$$

where the heat loss from the control volume to the ambient air is given as [48]

$$\dot{Q}_{loss} = \dot{Q}_{conv} + \dot{Q}_{count} \quad (21)$$

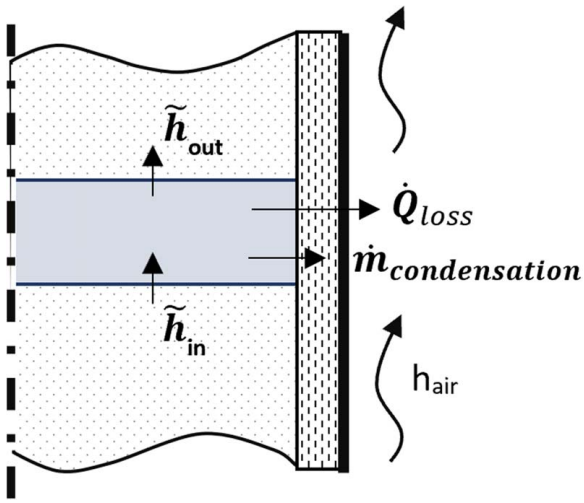

Fig. 4 Heat transfer of a control volume inside the heat-dissipating chimney

where $\dot{Q}_{conv}$ is the convection heat transfer between the moist air and inner surface of the chimney, which is expressed as

$$\dot{Q}_{conv} = h_{chim} A_{chim}^{surface-in} (T_{chim} - T_{air}) \tag{22}$$

The second term of the right-hand side in Eq. (21), $\dot{Q}_{count}$, is part of latent heat counted as heat loss [48], which is expressed as

$$\dot{Q}_{count} = \frac{\dot{Q}_{cd} \times U_{chim} A}{U_{chim} A + h_{chim} \times A_{chim}^{surface-in}} \tag{23}$$

where $\dot{Q}_{cd}$ is the latent heat, which is given as

$$\dot{Q}_{cd} = \dot{m}_{w-cd} * \tilde{h}_{fg} \tag{24}$$

The overall heat transfer coefficient from the inner wall to the ambient air is given as

$$U_{chim} A = \frac{1}{\frac{\ln\left(\frac{D_{chim-oD}}{D_{chim}}\right)/(2 * \pi * \Delta H_{chim})}{k_{chim}} + \frac{1}{h_{n-chim} A_{chim}^{surface-out}}} \tag{25}$$

where k_{chim} is the thermal conductivity of the material of the chimney. ΔH_{chim} is the length of a mesh. The convection heat transfer coefficient of moist air inside the chimney, h_{chim}, is determined from the Nusselt number ($h_{chim} = \mathrm{Nu}_{chim} \times k_{m-air}/D_{chim}$) (W/m^2-K).

The Nusselt number of heat transfer inside the chimney is given as a function of the Reynolds number [46]

$$\mathrm{Nu}_{chim} = \begin{cases} 4.36 & \mathrm{Re}_{chim} < 2300 \\ \dfrac{\left(\frac{f}{8}\right)(\mathrm{Re} - 1000)\mathrm{Pr}}{1 + 12.7\left(\frac{f}{8}\right)^{\frac{1}{2}}\left((\mathrm{Pr})^{\frac{2}{3}} - 1\right)} & 2300 < \mathrm{Re}_{chim} \end{cases} \tag{26}$$

In fact, for most of the simulated cases, the Reynolds number of flow inside the chimney is larger than 2300 which indicates that the flow is turbulent.

The natural convection heat transfer coefficient at the outer surface of the chimney is determined from the Nusselt number of the natural convection ($h_{n-chim} = \mathrm{Nu}_{n-chim} \times k_{air}/D_{chim-oD}$), which gives [49]:

$$\mathrm{Nu}_{n-chim} = \begin{cases} 0.59(\mathrm{Gr}_{n-chim} \times \mathrm{Pr}_{n-chim})^{\frac{1}{4}} & 1.43 \times 10^4 < \mathrm{Gr}_{n-chim} < 3 \times 10^9 \\ 0.0292(\mathrm{Gr}_{n-chim} \times \mathrm{Pr}_{n-chim})^{0.39} & 3 \times 10^9 < \mathrm{Gr}_{n-chim} < 2 \times 10^{10} \\ 0.11(\mathrm{Gr}_{n-chim} \times \mathrm{Pr}_{n-chim})^{\frac{1}{3}} & 2 \times 10^{10} < \mathrm{Gr}_{n-chim} \end{cases} \tag{27}$$

The mass conservation equation with a steady-state condition in a control volume in the chimney is given by the following equation:

$$0 = \dot{m}_{chim-in}^{total} - \dot{m}_{chim-out}^{total} - \dot{m}_{w-cd} \tag{28}$$

where $\dot{m}_{w-cd}$ represents the water condensation rate. The mass flowrate of air is assumed to be constant; hence, with $\dot{m}_{chim}^{total} = \dot{m}_{chim}^{vapor} + \dot{m}_{air}$, the equation can be simplified to the form of

$$\dot{m}_{w-cd} = \dot{m}_{chim-in}^{vapor} - \dot{m}_{chim-out}^{vapor} \tag{29}$$

Recall from Secs. 3.1 and 3.2, we design the system to make sure that air is fully humidified (RH = 1) in the water basin, when it reaches the entrance of the chimney. Therefore, moist air inside the chimney is saturated (RH = 1) anywhere. As a result, the mass flowrate of water vapor is given by the following equation:

$$\dot{m}_{chim}^{vapor} = \frac{P_{chim}^{sat-vapor} * V_{chim}}{R_{water} T_{chim}} \tag{30}$$

where the saturated pressure of water vapor is calculated using property equations in Sec. 3.6, and the volumetric flowrate of humid air is $V_{chim} = u_{chim} * A_{chim}^{cross}$.

3.6 Moist Air Properties Used in the Computation. The moist air properties are functions of the water vapor content, temperature, and pressure. The used correlations for all the properties of moist air are presented in this section.

Density: The density of moist air is given by the following expression in the form of,

$$\rho = \frac{1 + x}{R_{air} + R_{water} * x} * \frac{P}{T} \tag{31}$$

where $x = \dot{m}_{vapor}/\dot{m}_{air}$, represents the absolute humidity. $R_{air} = 287.68$ (J/kg-K) and $R_{water} = 461.54$ (J/kg-K) are the gas constant of air and water; P and T are the total pressure and temperature of the humid air.

Saturate vapor pressure: Based on Clausius–Clapeyron relation, the saturated vapor pressure of water vapor $P^{sat-vapor}$ (Pa) is given by August–Roche–Magnus equation [50]

$$P^{sat-vapor} = 6.11 \exp\left(\frac{17.625 \times (T - 273.15)}{(T - 273.15) + 243.04}\right) \times 100 \tag{32}$$

Therefore, the saturated vapor density of water vapor $\rho^{sat-water}$ (kg/m^3) is

$$\rho^{sat-water} = \frac{P^{sat-vapor}}{R_{water} T} \tag{33}$$

Heat capacity: Tsilingiris [50] recommended using the following expression to calculate the viscosity of a mixture of air and water vapor

$$Cp_m = x_a \times Cp_a + x_v \times Cp_v \tag{34}$$

where the mass fraction of air and water vapor are represented by the absolute humidity as $x_a = 1/(1 + x)$ and $x_v = x/(1 + x)$.

The heat capacity of air (J/kg-K) [46] and water vapor (J/kg-K) [51] are given, respectively, as

$$Cp_a = 1000 \times (Cp_{A4} \times T^4 + Cp_{a3} \times T^3 + Cp_{a2} \times T^2 + Cp_{a1} \times T + Cp_{a0}) \tag{35}$$

where the constants are: $Cp_{a4} = 0.1077024 \times 10^{-12}$, $Cp_{a3} = -0.4970786 \times 10^{-9}$, $Cp_{a2} = 0.7816818 \times 10^{-6}$, $Cp_{a1} = -0.284887 \times 10^{-3}$, and $Cp_{a0} = 1.03409$.

$$Cp_v = 1000(Cp_{v4} \times T^4 + Cp_{v3} \times T^3 + Cp_{v2} \times T^2 + Cp_{v1} \times T + Cp_{v0}) \tag{36}$$

where the constants are $Cp_{v4} = 3.247699333213341 \times 10^{-10}$, $Cp_{v3} = -2.998874574217572 \times 10^{-7}$, $Cp_{v2} = 1.005269619973656 \times 10^{-4}$, $Cp_{v1} = -0.013201538335907$, and $Cp_{v0} = 2.293445232271056$.

Viscosity: Based on Wilke's [52] investigation, Reid et al. [53] recommended using the following expression to calculate the viscosity of a mixture of dilute gases with multiple components

$$\mu = \frac{\mu_A}{1 + x_m \times \Phi_{AV}} + \frac{\mu_V}{1 + \frac{\Phi_{VA}}{x_m}} \tag{37}$$

where the molar fraction between vapor and air is represented by $x_m = x \times M_a/Mv$, and the interaction parameters are given by

$$\Phi_{AV} = \frac{\left(1 + \left(\frac{\mu_A}{\mu_V}\right)^{\frac{1}{2}} \left(\frac{M_{water}}{M_{air}}\right)^{\frac{1}{4}}\right)^2}{2 \times \sqrt{2} \times \left(1 + \frac{M_{air}}{M_{water}}\right)^{\frac{1}{2}}} \tag{38}$$

$$\Phi_{VA} = \frac{\left(1 + \left(\frac{\mu_V}{\mu_A}\right)^{\frac{1}{2}} \left(\frac{M_{air}}{M_{water}}\right)^{\frac{1}{4}}\right)^2}{2 \times \sqrt{2} \times \left(1 + \frac{M_{water}}{M_{air}}\right)^{\frac{1}{2}}} \tag{39}$$

The dynamic viscosity of air μ_A (Pa · s) and water vapor μ_V (Pa · s) based on temperature (K) is represented by the following equations [54]:

$$\mu_A = (\mu_{A0} + \mu_{A1} \times T + \mu_{A2} \times T^2 + \mu_{A3} \times T^3 + \mu_{A4} \times T^4)10^{-6} \tag{40}$$

where the constants are $\mu_{A4} = -6.2524 \times 10^{-12}$, $\mu_{A3} = 2.9928 \times 10^{-8}$, $\mu_{A2} = -5.7171 \times 10^{-5}$, $\mu_{A1} = 0.074582$, and $\mu_{A0} = 0.40401$

$$\mu_V = \frac{\sqrt{\frac{T}{647.27}}}{\mu_{V0} + \mu_{V1} \times \frac{647.27}{T} + \mu_{V2} \times \left(\frac{647.27}{T}\right)^2 + \mu_{V3} \times \left(\frac{647.27}{T}\right)^3} \times 10^{-6} \tag{41}$$

where the constants are $\mu_{V3} = -0.0036744$, $\mu_{V2} = 0.0105287$, $\mu_{V1} = 0.0177624$, and $\mu_{V0} = 0.0181583$.

Thermal conductivity: Based on the expression of Reid et al. [53] for the thermal conductivity of gas mixture, Tsilingiris [50] recommended the following expression to calculate the moist air thermal conductivity

$$k = \frac{k_A}{1 + x_m \times A_{AV}} + \frac{k_V}{1 + \frac{A_{VA}}{x_m}} \tag{42}$$

where Mason and Saxena [55] have recommended calculating the interaction parameters by

$$\mathrm{A}_{AV} = \frac{\left(1 + \left(\frac{k_{trA}}{k_{trV}}\right)^{\frac{1}{2}} \left(\frac{M_{air}}{M_{water}}\right)^{\frac{1}{4}}\right)^2}{2 \times \sqrt{2} \times \left(1 + \frac{M_{air}}{M_{water}}\right)^{\frac{1}{2}}} \tag{43}$$

$$\mathrm{A}_{VA} = \frac{\left(1 + \left(\frac{k_{trV}}{k_{trA}}\right)^{\frac{1}{2}} \left(\frac{M_{water}}{M_{air}}\right)^{\frac{1}{4}}\right)^2}{2 \times \sqrt{2} \times \left(1 + \frac{M_{water}}{M_{air}}\right)^{\frac{1}{2}}} \tag{44}$$

and

$$\frac{k_{trA}}{k_{trV}} = \frac{\mu_A}{\mu_V} \times \frac{M_{water}}{M_{air}} \tag{45}$$

$$\frac{k_{trV}}{k_{trA}} = \frac{\mu_V}{\mu_A} \times \frac{M_{air}}{M_{water}} \tag{46}$$

Substitute Eqs. (45) and (46) into Eqs. (43) and (44), one can see that $\mathrm{A}_{AV} = \Phi_{AV}$ and $\mathrm{A}_{VA} = \Phi_{VA}$. The conductivity of air k_A (W/m-K) and water k_V (W/m-K) based on temperature (°C) is given by the following expression [54]:

$$k_A = k_{A0} + k_{A1} \times T + k_{A2} \times T^2 + k_{A3} \times T^3 + k_{A4} \times T^4 \tag{47}$$

where the constants are $k_{A4} = -2.61420 \times 10^{-14}$, $k_{A3} = 2.85943 \times 10^{-12}$, $k_{A2} = -1.94021 \times 10^{-8}$, $k_{A1} = 7.83035 \times 10^{-5}$, and $k_{A0} = 2.43714 \times 10^{-2}$.

$$k_V = k_{V0} + k_{V1} \times T + k_{V2} \times T^2 + k_{V3} \times T^3 + k_{V4} \times T^4 \tag{48}$$

where the numerical constants are $k_{V4} = -3.17650 \times 10^{-12}$, $k_{V3} = 2.59524 \times 10^{-9}$, $k_{V2} = -3.23464 \times 10^{-7}$, $k_{V1} = 7.69127 \times 10^{-5}$, and $k_{V0} = 1.74822 \times 10^{-2}$.

Enthalpy: The saturated water vapor enthalpy $\tilde{h}_g$ (J/kg) as a function of temperature (°C) is given by the following expression:

$$\tilde{h}_g = H_{g4} \times T^4 + H_{g3} \times T^3 + H_{g2} \times T^2 + H_{g1} \times T + H_{g0} \tag{49}$$

where the constants are $H_{g4} = 9.943223804459140 \times 10^{-6}$, $H_{g3} = -0.010071020063398$, $H_{g2} = -0.009251431858592$, $H_{g1} = 1.838572076993385 \times 10^3$ and $H_{g0} = 2.501384672568149 \times 10^6$.

The saturated liquid water enthalpy $\tilde{h}_f$ (J/kg) as the function of temperature (°C) is given by the following expression:

$$\tilde{h}_f = H_{f4} \times T^4 + H_{f3} \times T^3 + H_{f2} \times T^2 + H_{f1} \times T + H_{f0} \tag{50}$$

where the constants are $H_{f4} = -3.051302634886905 \times 10^{-5}$, $H_{f3} = 0.011444749488429$, $H_{f2} = -1.133813902108926$, $H_{f1} = 4.220097984215571 \times 10^3$, and $H_{f0} = -71.602931323057460$.

The latent heat of water vaporization is $\tilde{h}_{fg}$ (J/kg), given as the function of temperature (°C)

$$\tilde{h}_{fg} = H_{fg4} \times T^4 + H_{fg3} \times T^3 + H_{fg2} \times T^2 + H_{fg1} \times T + H_{fg0} \tag{51}$$

where the constants are $H_{fg4} = 7.341023791486437 \times 10^{-6}$, $H_{fg3} = -0.013781106828722$, $H_{fg2} = 0.622151426394684$, $H_{fg1} = -2.376909569747994 \times 10^{-3}$, and $H_{fg0} = 2.500923458964323 \times 10^6$.

The above equations for enthalpy were from the book *Fundamentals of Engineering Thermodynamics* [51], which gives the applicable temperature range of $0 \leq T \leq 100\,^{\circ}\mathrm{C}$.

4 Algorithm and Computational Procedures for System Design

The computation for system design is to consider multiple parameters and decide a proper size of the water basin with given dimensions of chimney and temperatures of water and ambient air. The governing equations are applied to every control volume of airflow starting from the inlet/edge of the water basin and following the flow direction of air to march forward to the exit of the heat-dissipating chimney. The control volumes in the space above the water in the water basin are rings, with their diameters decreasing along the flow direction, as indicated in Fig. 2. The control volumes in the chimney are uniform along the height of the chimney. In the flow direction, the length of control volumes has been tested from 1.0 m to 1.0 cm for grid independence study. When the mesh size changes from 2.0 cm to 1.0 cm, the results of the total mass flowrate of air and total water evaporation rate vary within ±0.5%, while the total vapor condensation rate varies within ±0.1%. Therefore, a mesh size of 1.0 cm was chosen for the simulation.

To start the computation for all the governing equations for every control volume, we need to know some prescribed parameters including the water basin/chamber diameter D_{cham}, the distance δ between the water surface and inner surface of the glass cover, the chimney height H_{chim}, the chimney diameter D_{chim}, thermal conductivity of the chimney material, the water temperature T_{water} in the basin, and the ambient dry air temperature T_{dryair}.

The flowchart of computation, given in Fig. 5, reflects the algorithm and conditions of convergence to determine the water basin/chamber diameter and the water vapor condensation rate with prescribed parameters. The major steps of computations are as follows:

(1) Prescribe dimensions of chimney, temperatures of water and ambient air, and assume a small water basin area which will be updated to meet all the criteria in the next four steps.
(2) The flowrate or velocity of air entering the chamber is assumed from a small value and updated/changed increasingly to search for the velocities that allow the system to meet a criterion that the relative humidity of the airflow inside the water basin approaches 1.0 when it reaches to the inlet of the chimney. To do this, the mass transfer, water evaporation, and humidity of airflow in the water basin are calculated. It is noted that lower velocities of airflow can meet this criterion easily; therefore, a maximum air velocity meeting the criterion is searched out in this step. Here, the humidity criterion is based on the understanding that the moisture going to the air from the water basin should fully humidify the air.
(3) Using the velocities that could meet the humidity criterion in (2) to calculate the pressure losses of the flow in the entire system and then compare with the buoyancy-force-provided driving pressure from the chimney. To do this, the mass transfer, water condensation heat transfer, and humidity of airflow in the chimney are calculated. As the result, we can find the right velocity that the difference between the buoyancy-force-provided driving pressure and the pressure loss in the system is the smallest.
(4) Following *step (3)*, if the pressure loss from the system is less than the buoyancy-force-provided driving pressure at the selected velocity, the water basin area needs to be increased so that the pressure loss can become higher. With the increased water basin area, the computation goes back to *step (2)*, starting with new air velocities again and then moving forward to computations in *steps (3)* and *(4)*. Otherwise, if the pressure loss from the system is about the same as that of the buoyancy-force-provided driving pressure, the computation is converged, and the water basin area as well as the amount of condensed water is decided.
(5) Check the thermal energy usage per unit area in the water basin. If the used thermal energy per unit area is more than the solar energy density, the area of the water basin must be increased, and the computation will start over again. Another cause of the too-high energy usage per unit area could be an overestimation of the water temperature that was preset in the computation. Lowering the preset water temperature may also be considered in a new computation. On the other hand, the used thermal energy per unit area can be much less compared to the solar energy density. In this case, a higher water temperature should be considered at the beginning of a new computation.

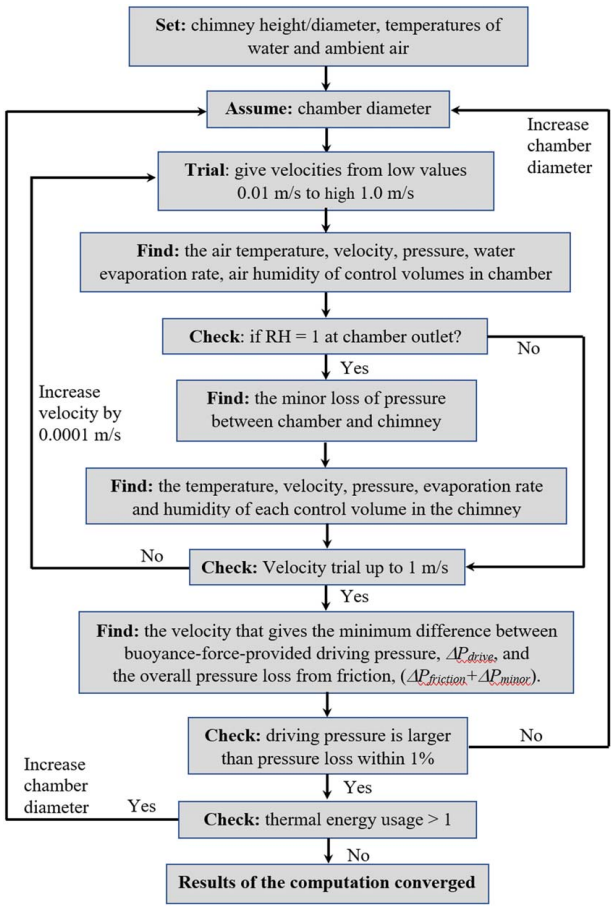

Fig. 5 Flow chart of computational procedures to decide the diameter of water basin to satisfy required criteria

Once a system is designed at typically selected chimney dimensions and water temperature, the desalination performance of the system should be checked at other water temperatures to verify that the system can also work well to satisfy the key requirement of relative humidity of 1.0 when the air flowing out of the water basin and entering the chimney.

5 Results and Discussions

Simulations using the developed model were first carried out for several cases with experimental data available from the authors' previous work [42]. The agreement of the simulation results with experimental data will be examined in Sec. 5.1 to validate the modeling and computer code, which will be applied to more simulations and optimization analysis in Secs. 5.2 through 5.4 to better understand the optimization designs of the desalination system.

5.1 Comparison of Computational Results to Experimental Data. The modeling and computer code were applied to the simulation of a desalination system that has been experimentally tested in the authors' previous work [42]. The chimney in the test was made of 6061 aluminum alloy (at a thermal conductivity of 167 W/(m°C)) with inner and outer diameters of $d_{in} = 0.254$ m and $d_o = 0.273$ m, and the height of $H = 3$ m. The water chamber in the experimental test was a square of 2.0 m by 2.0 m due to ease of fabrication. The polycarbonate glass cover (at a thermal conductivity of 0.22 W/(m°C)) of the chamber has a thickness of 4.49 mm, and the space between the glass cover and the water surface is 1.0 cm. Although strictly speaking, a round water chamber and a square chamber of the same area are not the same, it is still worthwhile to see if the simulation results are comparable to the experimental results to some extent.

To conduct a simulation analysis using the current modeling, an equivalent round chamber as that from the experimental test [42] was imagined. For the water surface area of 4 m^2, an equivalent diameter of a round chamber of $D = 2.257$ m was used in the simulation. Therefore, the entrance area of airflow for the experimental test system and the simulated system is the same. The ambient air

Table 1 Comparison of simulation results with previous experimental data [42]

	Simulated results			Experimental data			$\varepsilon = 100 \cdot$ (Sim.-Exp.)/Exp.		
T_{water} (°C)	$\dot{m}_{w-ev}^{total}$ (kg/s)	$\dot{m}_{w-cd}^{total}$ (kg/s)	$\dot{m}_{air}$ (kg/s)	$\dot{m}_{w-ev}^{total}$ (kg/s)	$\dot{m}_{w-cd}^{total}$ (kg/s)	$\dot{m}_{air}$ (kg/s)	ε_{ev} (%)	ε_{cd} (%)	$\varepsilon_{\dot{m}_{air}}$ (%)
40.37	6.42×10^{-4}	3.70×10^{-5}	1.51×10^{-2}	5.54×10^{-4}	3.78×10^{-5}	1.78×10^{-2}	13.7	−2.1	−18.1
45.68	9.47×10^{-4}	5.75×10^{-5}	1.81×10^{-2}	7.39×10^{-4}	5.89×10^{-5}	1.72×10^{-2}	22.0	−2.3	+5.3
45.35	9.28×10^{-4}	5.61×10^{-5}	1.80×10^{-2}	7.39×10^{-4}	5.83×10^{-5}	1.72×10^{-2}	20.4	−3.9	+4.5
47.82	1.08×10^{-3}	6.63×10^{-5}	1.92×10^{-2}	8.32×10^{-4}	6.69×10^{-5}	1.95×10^{-2}	23.3	−0.8	−1.8
47.65	1.07×10^{-3}	6.56×10^{-5}	1.91×10^{-2}	8.42×10^{-4}	6.62×10^{-5}	1.97×10^{-2}	21.6	−0.9	−3.4
49.16	1.18×10^{-3}	7.22×10^{-5}	1.98×10^{-2}	9.78×10^{-4}	7.38×10^{-5}	2.35×10^{-2}	17.0	−2.1	−18.6
49.19	1.18×10^{-3}	7.24×10^{-5}	1.98×10^{-2}	9.37×10^{-4}	7.49×10^{-5}	2.13×10^{-2}	20.7	−3.4	−7.5

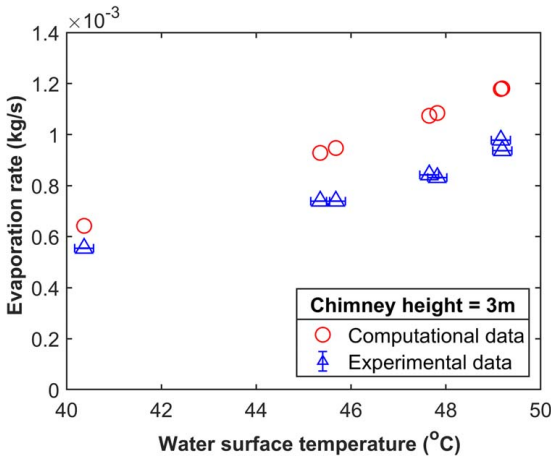

Fig. 6 Total evaporation rate of the test and simulated cases at various water surface temperatures

temperature is 23 °C, which is the laboratory experimental condition [42].

The simulated results of the water evaporation rate in the chamber, the water vapor condensation rate in the heat-dissipating chimney, and the airflow mass flowrate at the entrance of the chamber are given in Table 1 for comparison with that from the experimental work [42].

In Fig. 6, the water evaporation rates at water temperatures from 40 °C to 49 °C in the chamber from experimental test and numerical simulation are compared. The computational results showed to be 13.7–23.3% higher than that of the experimental data for all four cases of different water surface temperatures. In Fig. 7, the water vapor condensation rates in heat-dissipating chimneys are compared between experimental tests and numerical simulations for cases of water temperature of 40–49 °C in the chamber. The computational results showed a maximum of 3.9% lower than that of the experimental data. In Fig. 8, the airflow mass flowrate at the inlet of the chamber is given for both the experimental tests and numerical simulation for cases of water temperature of 40–49 °C in the chamber. The computational results showed to have a maximum of 18.6% deviation from that of the experimental data.

It needs to point out that in the experimental test, any disturbance of airflow can enhance the convection heat transfer from the surface of the chimney to the ambient air or from the surface of the glass cover to the ambient air. Therefore, the water evaporation rate may be lower compared to the simulation results due to potentially more heat loss in the actual experiment. However, for the water vapor condensation rate, the experimental results may be higher than that of simulation results due to the possibility of more heat loss from the chimney to ambient air. These features are exactly observed from the comparison of the experimental results with the simulated results in Figs. 6 and 7.

Finally, it is also noted that the empirical equations of heat and mass transfer coefficients from most textbooks can have a deviation from ±15% to ±30% [45] with experimental results. Therefore, the maximum 23% difference between the simulation results against the experimental test results in this work is acceptable, which is strong evidence that the current modeling analysis and simulation are reasonably good and reliable. We can conclude that the modeling and simulation can be a reliable tool for the design and optimization of the water basin with given dimensions of heat-dissipating chimney and the temperatures of the water and ambient air. The design optimization can help engineers to maximize clean water production using the currently proposed desalination system.

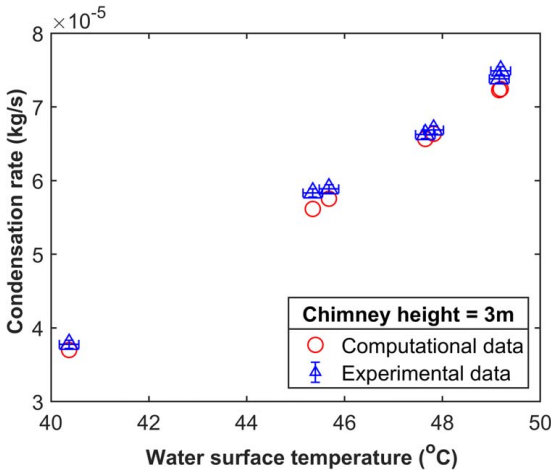

Fig. 7 Total vapor condensation rate from the test and simulated cases at various water surface temperatures

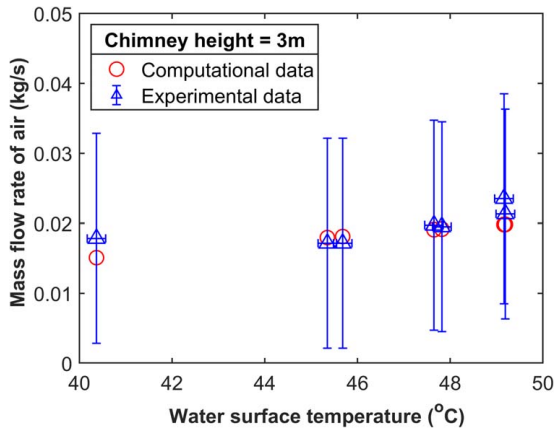

Fig. 8 Inlet mass flowrate of air of the test and simulated cases at various water surface temperatures

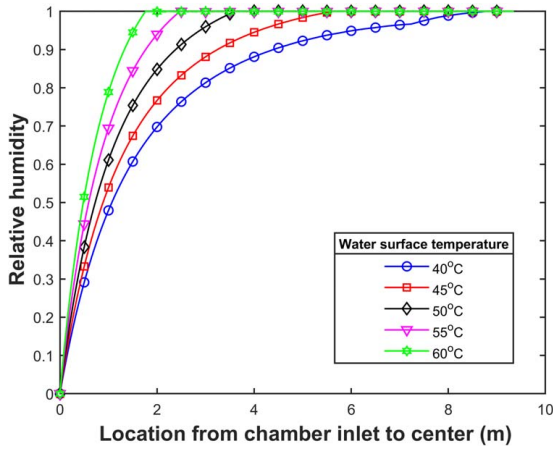

Fig. 9 Relative humidity at locations inside the chamber under different water surface temperatures ($d_{chim} = 0.3$ m, $H_{chim} = 16$ m, $D_{cham} = 19$ m, $\delta = 0.05$ m)

The results of more simulations for design and parametric studies are presented in the next four sections. Section 5.2 includes the computational results of chamber design at prescribed chimney size and water temperature, the details of the relative humidity of air in the chamber, the airflow velocities, water evaporation rate in the chamber, water vapor condensation rate in the heat-dissipating chimney, and the variation of these parameters with different water temperatures. In Sec. 5.3, the effects of the chimney height at different chimney diameters on the flowrate of air as well as the water evaporation and condensation rate are reported and discussed. In Sec. 5.4, the details of the optimization of water basin/chamber dimensions at different chimney heights and diameters will be presented.

5.2 Basin/Chamber Design With Given Chimney and Operation at Different Water Temperatures. Optimization for system design was carried out using the developed MATLAB code following the modeling and algorithm in Sec. 4. It is important to note that a design for the solar collection chamber requires two criteria. First, the relative humidity at the outlet of the basin/chamber must reach 100%. This is important since it allows fully humidified air entering the heat-dissipating chimney to condense the maximum amount of vapor for the collection of distilled water. Second, the chamber diameter must be large enough to provide sufficient thermal energy to satisfy the requirement of latent heat for water evaporation as well as the heat loss from the chamber to ambient air. On the other hand, the energy density needed for the system shall not be larger than the actual solar energy density.

The prescribed conditions include the chimney height of 16 m and inner/outer diameters of 0.3 m/0.32 m, the temperature of ambient air of 25 °C, and the space between the water surface and cover glass of 0.05 m. The chimney material is aluminum with thermal conductivity of 167 W/(m°C). The polycarbonate glass cover has a thickness of 4.49 mm with thermal conductivity of 0.22 W/(m°C). The water temperature was set at 40 °C for the design. The design analysis and computation found that the water basin diameter should be 19 m to satisfy the criterion that the humidity of air reaches 1.0 when air flows out of the chamber.

With the designed dimensions of the system, computations at different temperatures could be conducted. Detailed information from the simulation, such as the air flowrate, the relative humidity, the evaporation rate, and condensation rate, could be obtained for several cases of different water temperatures. It is noted that at other water temperatures, the optimal basin diameter will be different. However, for temperatures higher than 40 °C, the optimal basin diameter will be smaller than 19 m if the chimney is the same. Therefore, the relative humidity can reach 1.0 in the water basin with a diameter of 19 m at higher water temperatures and heat flux.

Figure 9 shows the local relative humidity of air along the flow direction from the water basin/chamber inlet to the center before entering the chimney. At higher water temperatures, the relative humidity was found reaching 1.0 earlier before the flow approaches the center of the chamber. This means that starting from the chamber inlet, the distance required to fully humidify the air decreases when the water temperature increases. It is understandable that the latent heat of water required for evaporation decreases when the water temperature increases. Additionally, the water vapor concentration at the water surface increases with the temperature, and therefore, the mass transfer rate (evaporation rate) at higher temperatures is higher, which is seen in Fig. 10(*a*).

Figure 10 shows the local water evaporation rate in the chamber and local condensation rate in the heat-dissipating chimney. We see that the evaporation rate at the entrance region of the chamber is high but gradually decreases, and then, there is a significant increase at a location close to the center of the chamber. Looking at the local Reynolds number, we found the value passing 2300 and the flow becomes turbulent flow at this location, which results in a significant increase in mass transfer or evaporation rate. At higher water temperatures, the evaporation rate is high and so for the condensation rate in the heat-dissipating chimney. The local condensation rate decreases at higher locations of the chimney. This is because the temperature difference between the humid air inside the

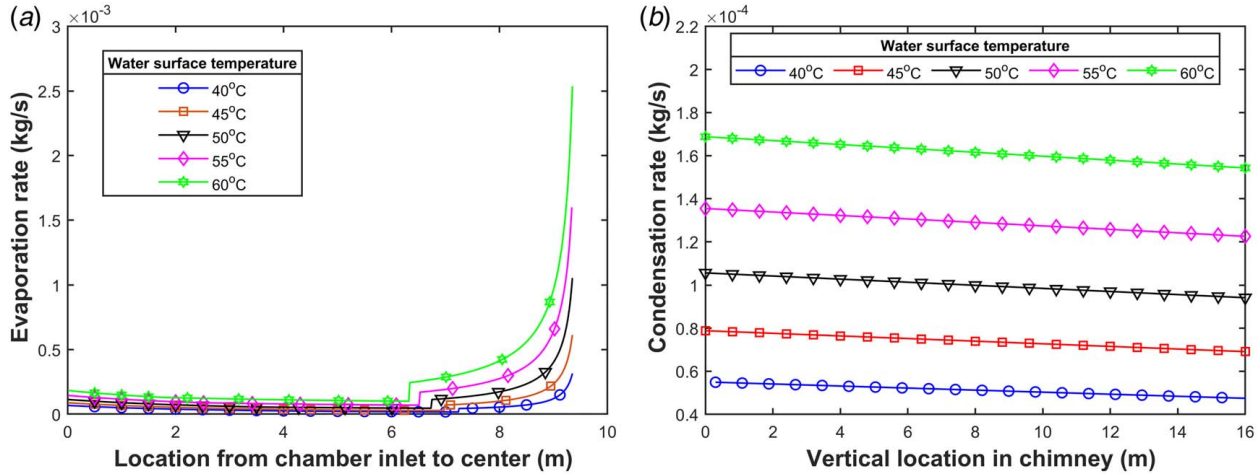

Fig. 10 Local water evaporation rate and water vapor condensation rate per unit area in the flow directions of air ($d_{chim} = 0.3$ m, $H_{chim} = 16$ m, $D_{cham} = 19$ m, $\delta = 0.05$ m)

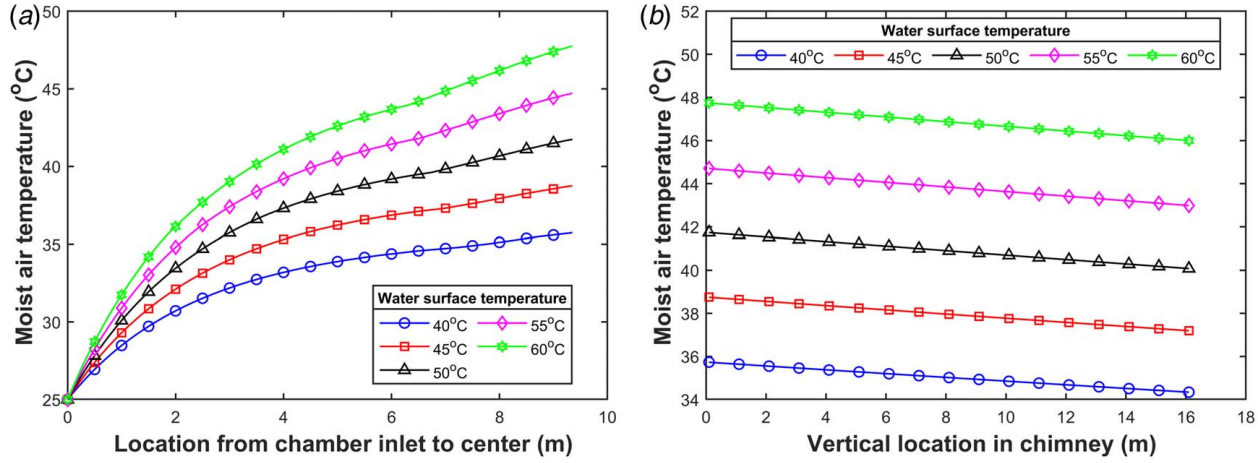

Fig. 11 Local moist air temperature inside the system ($d_{chim} = 0.3$ m, $H_{chim} = 16$ m, $D_{cham} = 19$ m, $\delta = 0.05$ m)

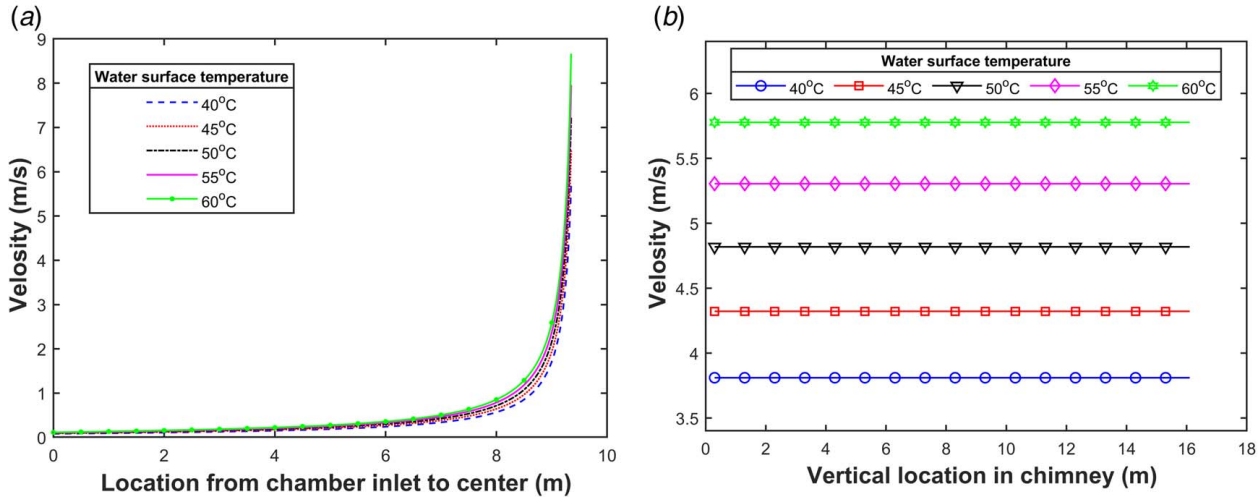

Fig. 12 Velocity of moist airflow along the flow direction in water basin and in the heat-dissipating chimney ($d_{chim} = 0.3$ m, $H_{chim} = 16$ m, $D_{cham} = 19$ m, $\delta = 0.05$ m)

chimney and the ambient air is getting less and heat dissipation from the chimney decreases at higher locations. The humid air temperature in the chamber and the heat-dissipating chimney is shown in Fig. 11.

While the water surface temperature is constant, the heat transfer between the water surface and the air results in the increase of the air temperature as shown in Fig. 11. The moist air temperature at the chamber outlet could reach 36 °C and 48 °C, respectively, at the water surface temperatures of 40 °C and 60 °C. The increase in the temperature difference between the humid air inside the chimney and the ambient air causes an increase in the heat transfer and thus a greater condensation rate, as shown in Fig. 10(*b*).

The airflow is laminar from the entrance of the chamber to a certain length. However, the flow velocity increases in the chamber toward the exit of the chamber, as shown in Fig. 12(*a*), and therefore, the flow will become turbulent when it gets close to the exit of the chamber. The flow velocity inside the chimney does not change significantly as shown in Fig. 12(*b*), and the Reynolds number is larger than 2300, as a turbulent flow. For the case with higher water temperature, the temperature difference between the humid air inside the chimney and the ambient air outside of the chimney is large, and therefore, there is a greater driving force for the flow or stronger chimney effect, which makes a greater flowrate of air through the system.

The local pressure of the humid airflow in the chamber and the chimney are shown in Fig. 13. Because of the friction loss of pressure, the local pressure decreases in the chamber and the chimney. When the airflow approaches the exit of the chamber and goes to the chimney with a change of flow direction, the pressure drop is significant, which is clearly shown in Fig. 13(*a*). The pressure loss of the humid airflow in the chimney is linear. Because of the large flowrate at higher water temperatures, the pressure loss is more significant for the cases of higher water temperature.

It is worth noting that the above-discussed results have shown reasonable and correct physical phenomenon in the desalination system, which is another verification of the modeling. For further studies, the computer code has been used to compute more cases for optimization of the dimensions of the chimney with given chambers and water temperature conditions.

5.3 Optimization of the Chimney Height for Given Chamber. In this section, we would like to search for optimal chimney height at a properly pre-decided water chamber diameter. There are three chimney inner diameters considered, 0.2 m, 0.3 m, and 0.4 m. The space between the water surface and cover glass is kept at $\delta = 0.05$ m, and the ambient air temperature is 25 °C. The investigated temperatures of the water surface range from 40 °C to 60 °C.

The pre-decision of a chamber diameter is made based on analyses and computation at a water temperature of 40 °C. We first give a relatively small chamber diameter, and then chose more than ten different chimney heights and conduct computations to check if

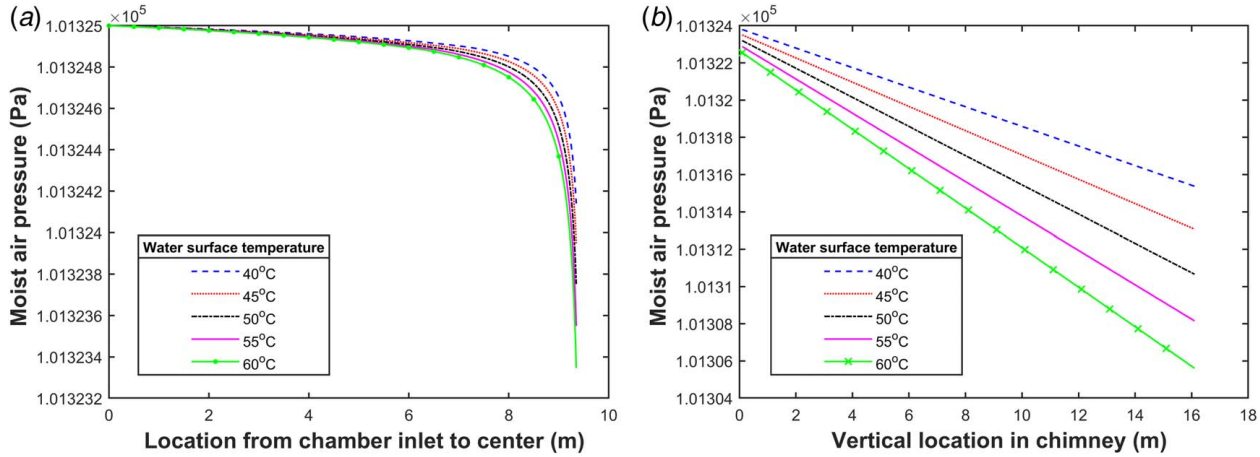

Fig. 13 Pressure along the flow direction inside the system ($d_{chim} = 0.3$ m, $H_{chim} = 16$ m, $D_{cham} = 19$ m, $\delta = 0.05$ m)

the relative humidity of air can reach 1.0 in the water chamber at every trial chimney height. If the relative humidity of air cannot reach 1.0 at any trial chimney height, the chamber diameter will be enlarged until satisfaction is accomplished. For a chimney inner diameter of 0.2 m, 0.3 m, and 0.4 m and a number of chosen chimney heights, the obtained water chamber diameter is 11 m, 19 m, and 24 m, respectively. At these determined chamber diameters, the obtained parameters of airflow velocity, total water evaporation rate, and total water vapor condensation rate are presented for different water temperatures. At water temperatures greater than 40 °C, the selected chamber diameter based on the water temperature of 40 °C is still sufficiently large for the relative

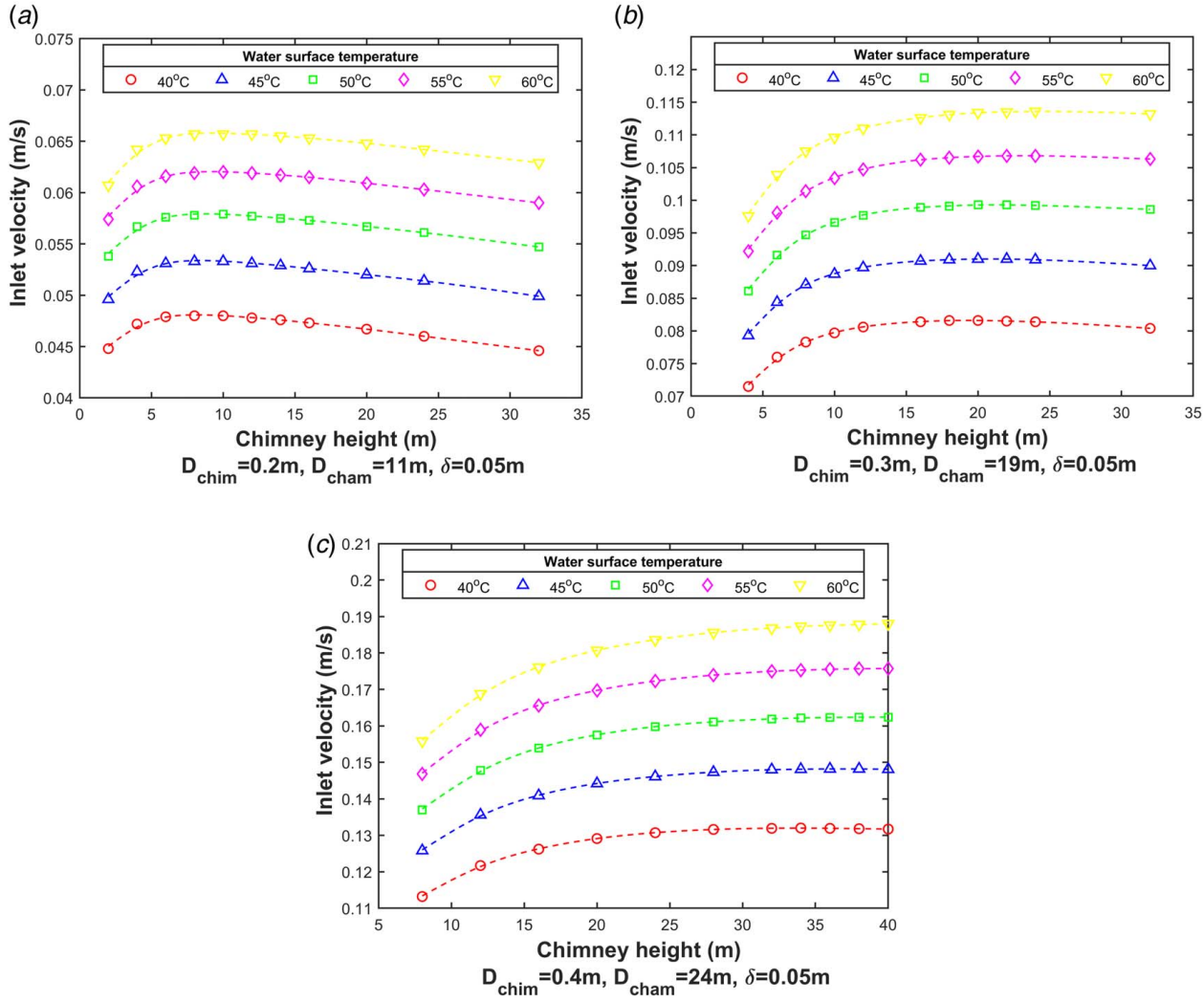

Fig. 14 Chamber inlet velocity of air at various conditions of chamber diameters, chimney heights, and water temperatures

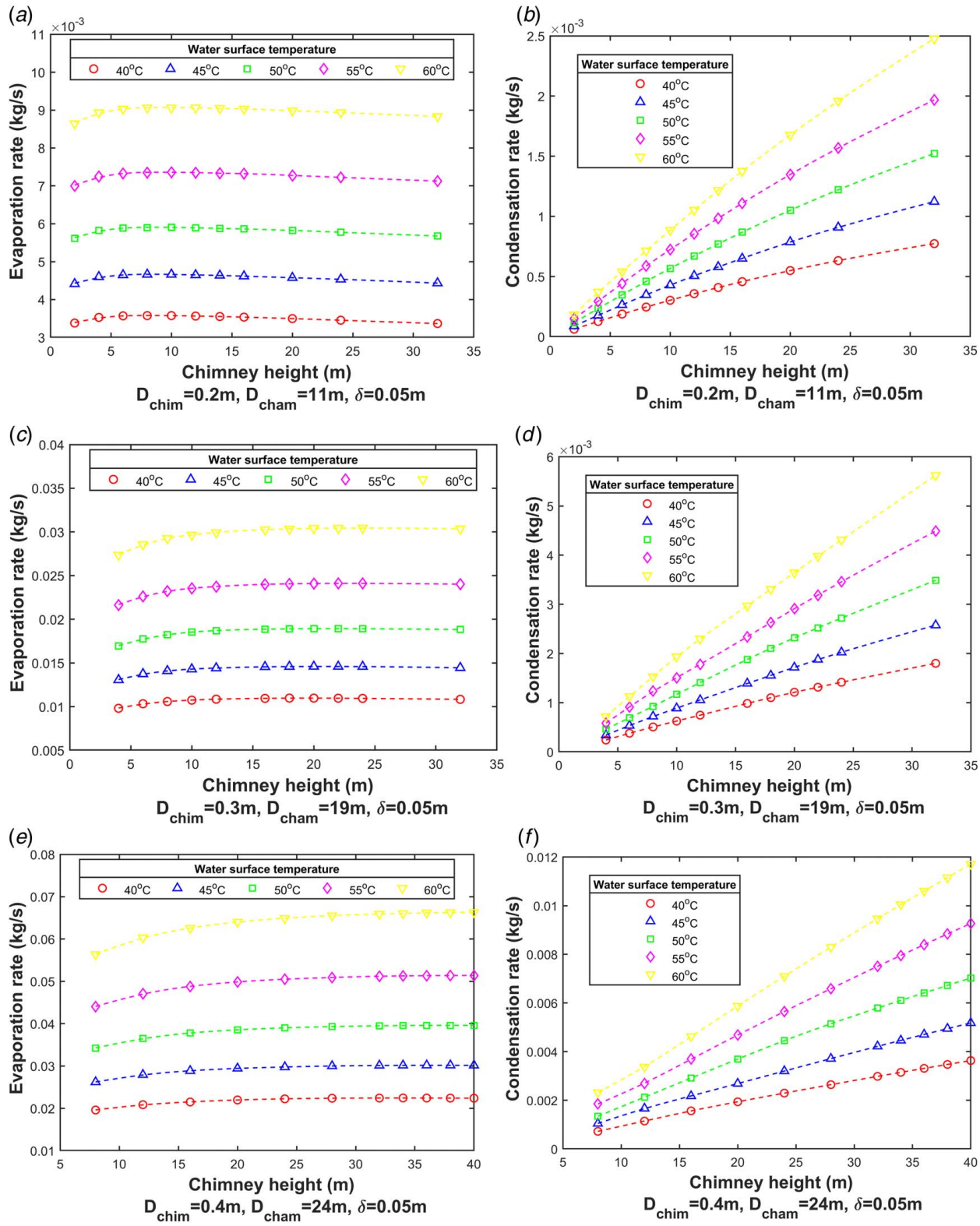

Fig. 15 Total evaporation rate and condensation rate at various conditions of chamber diameters, chimney heights, and water temperatures

humidity of the air to reach 1.0. The chimney height that can result in the highest air flowrate for each water chamber is then determined.

Figure 14 shows the inlet air velocities for cases of different chimney heights at different water temperatures and the predetermined constant water chamber diameters. For the chimney diameter of 0.2 m in Fig. 14(*a*), there is a maximum inlet air velocity appeared at a chimney height of 8 m. If a taller chimney is used, the air flowrate will decrease due to larger friction loss even if the taller chimney should provide more driving force for the flow. This is indeed due to the relatively large friction loss in a small-diameter chimney. It is also worth noting that the chimney is heat dissipating, and therefore, the flowrate will not always increase with the increase of chimney height. This is because the taller chimney helps the

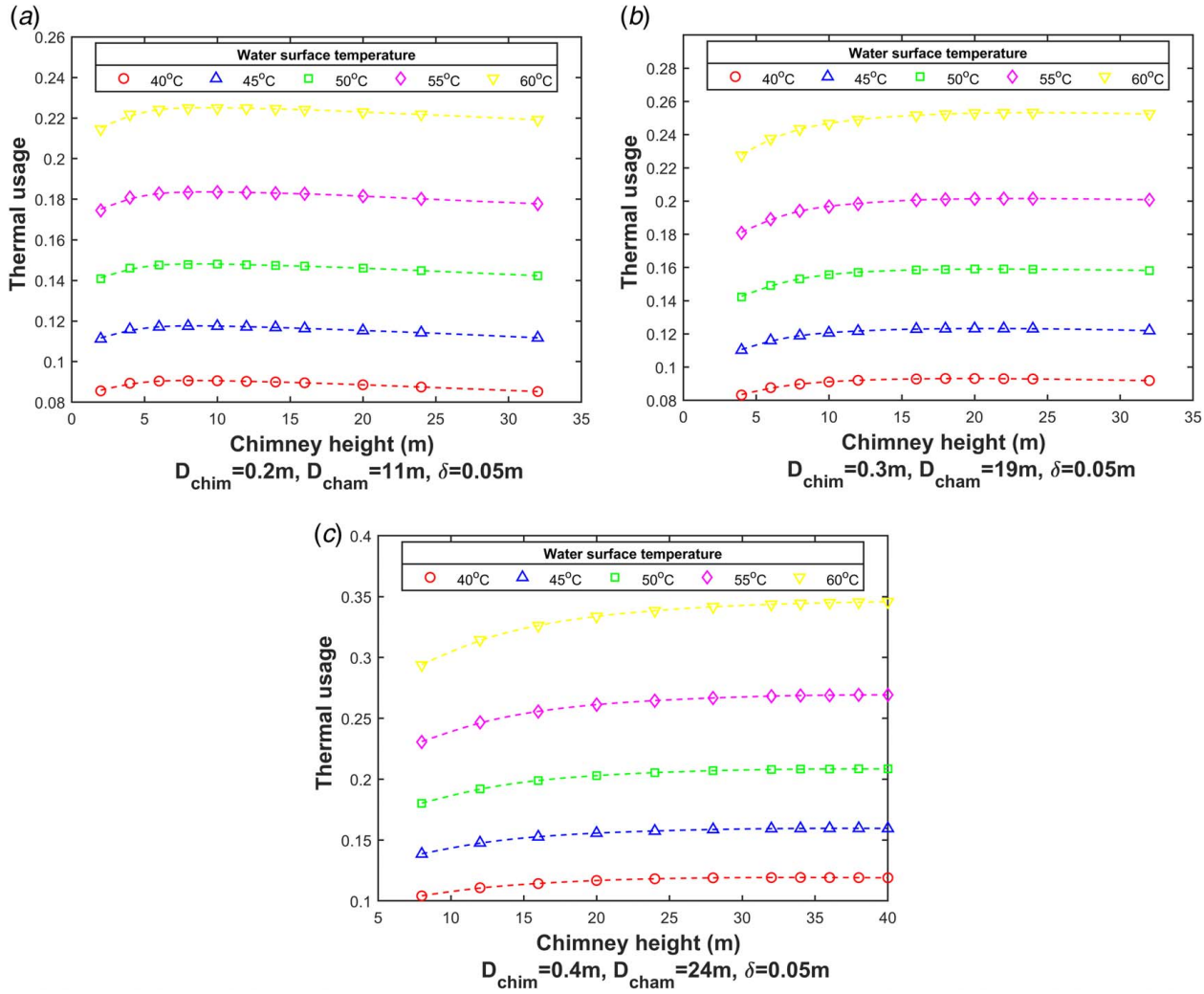

Fig. 16 Thermal usage at different conditions of water temperature, water chamber diameter, and chimney diameter and height

cooling of the humid air in the chimney, and thus, the buoyance force in the upper part of the chimney decreases. This feature is different from that of the adiabatic chimney in solar chimney power systems. In the latter case, the increase in chimney height (as greater as 200 m [33]) could still contribute to the higher driving force and thus greater airflow for power generation.

When the chimney diameter increased to 0.3 m, the inlet air velocities can be greater and the maximum air flow occurs at the case of chimney height of 18 m, as shown in Fig. 14(*b*). This is because, at a larger chimney diameter, the friction loss is much smaller which allows more airflow to pass through the system. Further evidence is seen for the case of a chimney diameter of 0.4 m, shown in Fig. 14(*c*), where a chimney height can be 34 meters to reach a maximum air flowrate.

It needs to point out that there is a critical height of the chimney that introduces the maximum airflow into the system. Any chimney with a height greater than the critical height could have decreased flowrate of air. However, for a chimney taller than the critical length, the extra length could still help to cool water vapor in the chimney and therefore increases the condensation rate or water production rate.

The total water evaporation rate in the water chamber and the total vapor condensation rate in the chimney are given in Fig. 15 for various chimney heights at the determined chamber and chimney diameter. With a fixed diameter of the chamber, the water evaporation rate in the chamber does not change dramatically with the change in chimney height. This is because the evaporation is tightly related to the airflow rate as shown in Fig. 14. The slight change of water evaporation rate is due to the change of air flowrate at different heights of chimney. However, the water vapor condensation rate increases with the increase in chimney height since a taller chimney offers more heat transfer surface area for the vapor condensation.

The results in this section indicate that the chimney diameter is an important factor in determining the maximum airflow rate in the desalination system. With a small chimney diameter, the maximum air flowrate is available at a small critical chimney height, while at a large chimney diameter, the air flowrate peaks at a greater critical chimney height. Increasing the chimney height being greater than the critical height will not cause an increase in the flowrate of air but only cause an increase in the total condensation rate. It needs to point out that in the above analyses, the predecided water chamber diameter is always sufficient to guarantee that the relative humidity of the air in the water chamber can reach 1.0 when it flows to the exit of the chamber.

5.4 Optimization of Water Chamber Size Considering Certain Thermal Energy Usage in the Water Evaporation. It is understandable that at different water temperatures, the water evaporation process consumes different amounts of thermal energy or different percentages of solar irradiance. This means that different water temperature is correlated to different solar energy density. For example, in the early morning and late afternoon, the solar energy density is low so that the

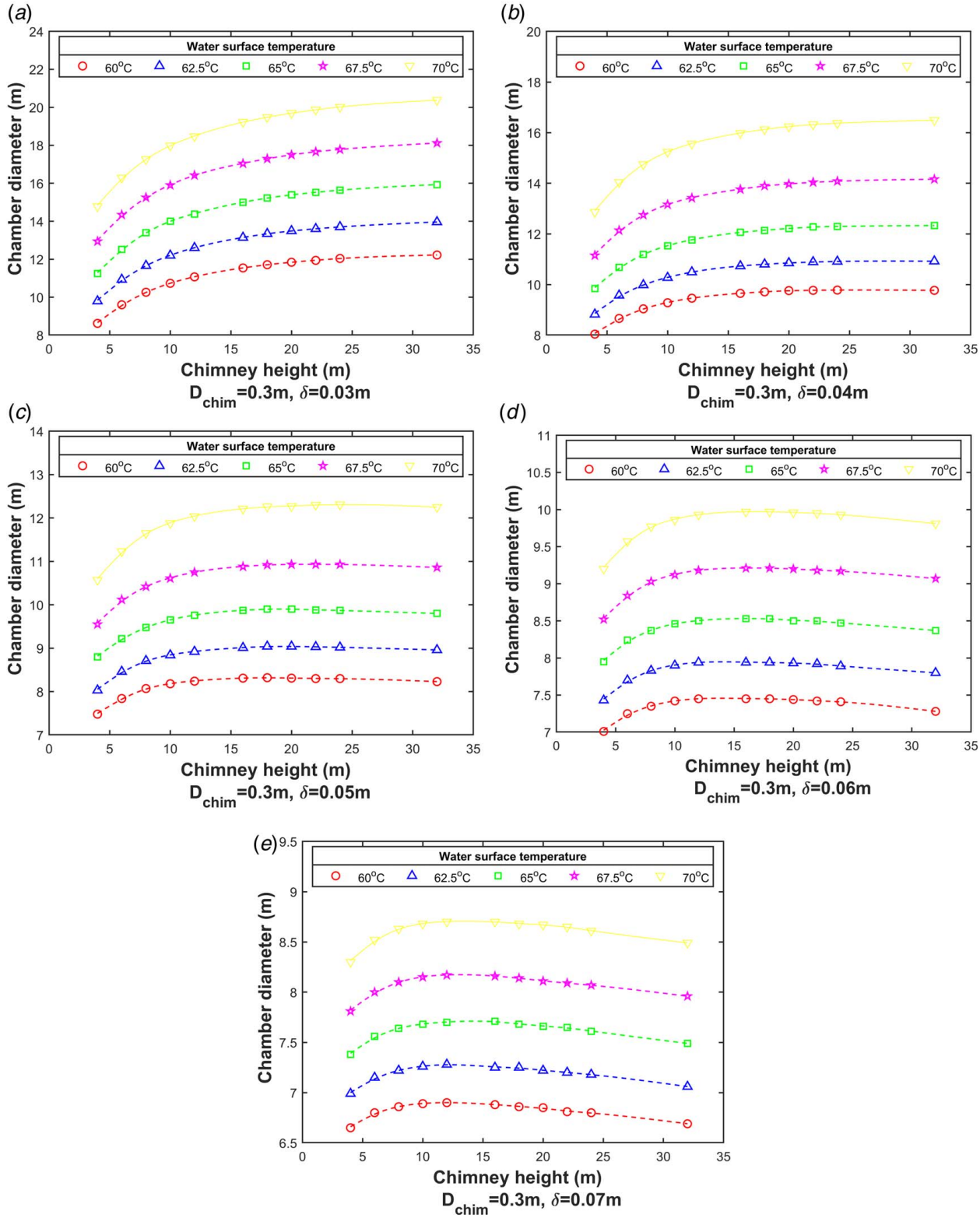

Fig. 17 Optimized chamber diameter at different chimney heights at five different water temperatures

water temperature can be low; while in the period of about 3 h before and after noon time, the solar energy density is high and therefore the water temperature is also high. The maximum solar irradiance at the earth's surface is typically 1000 W/m^2 and considering the reflection of sunlight at the surface of the glass and the surface of the water, a reasonable amount of solar energy absorbed by the water is assumed to be 600 W/m^2, which has been reported by multiple researchers [37]. From hereafter, we call the used percentage of energy density from 1000 W/m^2 as the thermal usage.

The thermal usage of the cases analyzed in Sec. 5.3 can be easily calculated from the computations. If the calculated thermal usage is lower than 100%, it means the assumed water temperature is correlated to a lower heat flux of less than 1000 W/m^2. On the other hand,

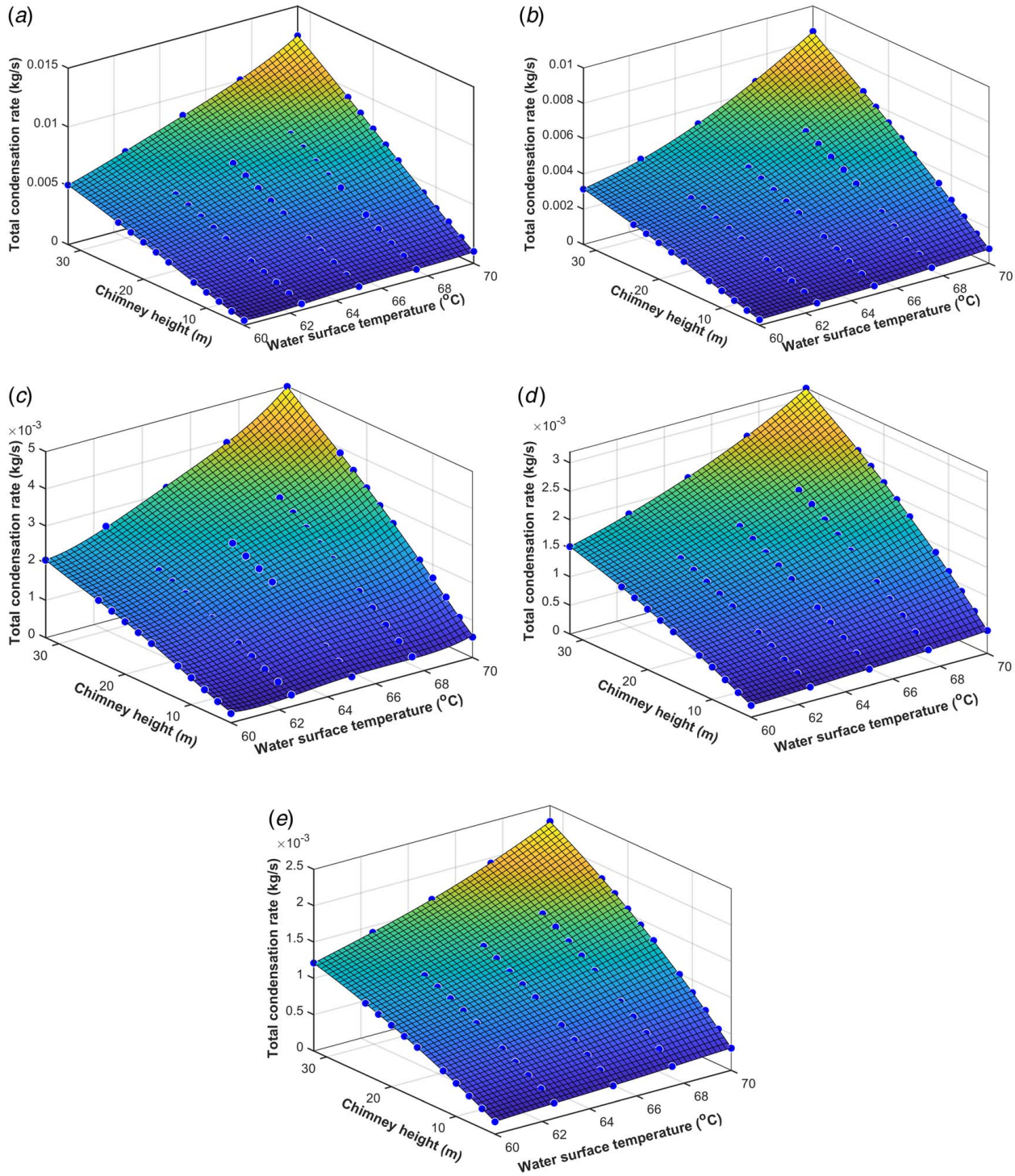

Fig. 18 Total water vapor condensation rate as a function of water surface temperature and the chimney height that determines the optimized water chamber diameters at a given space between the water surface and the cover glass: (*a*) $d_{chim} = 0.3$ m, $\delta = 0.03$ m, (*b*) $d_{chim} = 0.3$ m, $\delta = 0.04$ m, (*c*) $d_{chim} = 0.3$ m, $\delta = 0.05$ m, (*d*) $d_{chim} = 0.3$ m, $\delta = 0.06$ m (e) $d_{chim} = 0.3$ m, $\delta = 0.07$ m

to ensure high thermal usage, it must be correlated to a higher water temperature and large air flowrate.

For all the cases presented in Sec. 5.3, the values of thermal usage were examined here. Shown in Fig. 16 are the plots of the thermal usage values at various conditions including water temperatures, chimney diameter and height, pre-determined chamber diameters, and the ambient air temperature of 25 °C.

It is observed that the energy usage of these cases in Fig. 16 is low, ranging from 8% to 35%. These cases can be viewed as operating cases at low energy density, corresponding to the time in the morning or late afternoon when the solar energy density is relatively low. Energy usage is significantly affected by the chimney height if the height is less than the critical height. For chimney height above the critical height, it only has a slight effect on the flowrate and energy usage. At the critical chimney height for each case of chamber diameter, the air flowrate reaches the maximum, and therefore, the energy usage reaches the maximum.

Table 2 Coefficients Q_i from curve-fitting for $\dot{m}_{w-cd}^{total}$ using Eq. (52)

δ (m)	0.03 m	0.04 m	0.05 m	0.06 m	0.07 m
Q_1	3.503445E + 00	−1.814635E + 00	2.608156E + 00	−1.856838E-01	−9.586925E-01
Q_2	−2.097669E-01	1.071509E-01	−1.618236E-01	1.136565E-02	5.935649E-02
Q_3	−1.893370E-02	2.222738E-02	−5.825376E-03	−9.792038E-04	−1.654257E-03
Q_4	4.704402E-03	−2.365653E-03	3.760605E-03	−2.611004E-04	−1.376956E-03
Q_5	8.398771E-04	−9.757109E-04	2.944265E-04	5.902076E-05	8.203227E-05
Q_6	7.173444E-05	−5.069639E-05	−9.087414E-06	−1.138595E-05	−2.565337E-06
Q_7	−4.683432E-05	2.315289E-05	−3.879259E-05	2.668432E-06	1.418498E-05
Q_8	−1.261245E-05	1.392777E-05	−5.000229E-06	−1.149380E-06	−1.365775E-06
Q_9	−1.929398E-06	2.077285E-06	3.384894E-07	3.429618E-07	9.786286E-08
Q_{10}	−3.420421E-07	−5.732854E-07	−5.115437E-08	2.934243E-08	−1.073235E-08
Q_{11}	1.746173E-07	−8.479346E-08	1.498621E-07	−1.024123E-08	−5.475631E-08
Q_{12}	6.480538E-08	−6.402013E-08	2.888945E-08	7.602215E-09	7.879025E-09
Q_{13}	1.527066E-08	−1.684419E-08	−3.057270E-09	−2.667993E-09	−1.028290E-09
Q_{14}	−8.351399E-10	−2.052203E-11	3.743301E-10	−6.125178E-10	1.310225E-10
Q_{15}	4.808847E-09	7.937855E-09	3.174893E-10	1.243643E-10	5.160012E-11

Table 3 Coefficients B_i obtained from curve-fitting for Q_i as a function of δ in Eq. (53)

i (Q)	B_1	B_2	B_3	B_4	B_5
Q_1	3.048916E + 08	−6.228902E + 07	4.636235E + 06	−1.486424E + 05	1.731672E + 03
Q_2	−1.879009E + 07	3.838325E + 06	−2.856454E + 05	9.156235E + 03	−1.066428E + 02
Q_3	−3.994317E + 05	8.409417E + 04	−6.493727E + 03	2.175205E + 02	−2.661979E + 00
Q_4	4.338479E + 05	−8.861207E + 04	6.593329E + 03	−2.113006E + 02	2.460370E + 00
Q_5	1.735184E + 04	−3.666875E + 03	2.843514E + 02	−9.568908E + 00	1.176665E-01
Q_6	1.607937E + 03	−3.116460E + 02	2.175403E + 01	−6.463667E-01	6.937832E-03
Q_7	−4.447969E + 03	9.083541E + 02	−6.757534E + 01	2.165133E + 00	−2.520365E-02
Q_8	−2.493012E + 02	5.290305E + 01	−4.121606E + 00	1.394107E-01	−1.723670E-03
Q_9	−4.885164E + 01	9.486897E + 00	−6.640115E-01	1.979920E-02	−2.133136E-04
Q_{10}	−1.577820E + 00	2.851901E-01	−1.792975E-02	4.563710E-04	−4.038528E-06
Q_{11}	1.708532E + 01	−3.488595E + 00	2.594777E-01	−8.311728E-03	9.672602E-05
Q_{12}	1.179441E + 00	−2.515062E-01	1.970182E-02	−6.704328E-04	8.344349E-06
Q_{13}	3.950271E-01	−7.698225E-02	5.413469E-03	−1.624132E-04	1.762547E-06
Q_{14}	−3.643130E-02	7.544919E-03	−5.712689E-04	1.867804E-05	−2.212348E-07
Q_{15}	4.981944E-02	−9.703864E-03	6.801734E-04	−2.026738E-05	2.181329E-07

More simulations have been carried out to look at the dimensions of the chamber and chimney that can have energy usage of up to 60%. It was found that if 600 W/m^2 of energy is used and water temperature reaches 60 °C, the needed chamber diameters can be less than that shown in Fig. 16 at a chimney diameter of 0.3 m or above. Figure 17 shows the obtained results at all the studied chimney heights. Under the same heat flux of 600 W/m^2, if the water temperature is higher than 60 °C, the chamber diameter needs to be larger than that corresponding to the case of 60 °C. These results also imply that if the system can get 60% of the solar energy used for water evaporation, the water temperature in the basin should be able to reach 60 °C or above. From the perspective of system design optimization, the combinations of the chimney diameters, heights, and chamber diameters in Fig. 17 are optimal at the given water temperatures and heat flux around 600 W/m^2. If a heat flux is lower than 600 W/m^2 and the temperatures are still the same from 60 °C to 70 °C, the chamber diameters must be greater than the values in Fig. 17.

Figure 17 also gives the optimized water chamber diameters at different spaces between the water surface and the cover glass, under the condition that the solar energy usage reaches 60% of 1000 W/m^2. The optimized chamber diameter becomes less if the space between the water surface and the glass cover increases. As shown in Figs. 17(*a*) and 17(*b*), for smaller spaces of $\delta = 0.03$ m and $\delta = 0.04$ m, the chamber diameter could be larger than 8 m. On the other hand, as shown in Figs. 17(*d*) and 17(*e*), for larger spaces of $\delta = 0.06$ m and $\delta = 0.07$ m, the chamber diameter can be significantly less. This is because, with the larger spaces and more airflow, the heat and mass transfer becomes better, and therefore, the relative humidity of air can still approach 1.0 with no need for a larger chamber diameter. The chamber diameter increases with the increase in chimney height when the chimney height was below the critical height. However, a further increase in chimney height beyond the critical height does not cause more increase in the chamber diameter.

For the above-discussed cases, at given water temperatures and chimney height, the chamber diameters are determined. Therefore, further, the total water evaporation rate and water vapor condensation rate can be determined. Consequently, the total vapor condensation rate in the heat-dissipating chimney can be drawn as a function of the water temperature and the chimney height, as shown in Fig. 18.

For every contour shown in Fig. 18, a curve-fitting could be made for the condensation rate $\dot{m}_{w-cd}^{total}$ as a function of water temperature and chimney height. The curve-fitted two-variable function is expressed in the form of

$$\begin{aligned}\dot{m}_{w-cd}^{total} = {} & Q_1 + Q_2 \times T_{water} + Q_3 \times H_{chim} + Q_4 \times T_{water}^2 + Q_5 \times T_{water} \\ & \times H_{chim} + Q_6 \times H_{chim}^2 + Q_7 \times T_{water}^3 + Q_8 \times T_{water}^2 \times H_{chim} \\ & + Q_9 \times T_{water}^* H_{chim}^2 + Q_{10} \times H_{chim}^3 + Q_{11} \times T_{water}^4 \\ & + Q_{12} \times T_{water}^3 \times H_{chim} + Q_{13} \times T_{water}^2 \times H_{chim}^2 + Q_{14} \\ & \times T_{water} \times H_{chim}^3 + Q_{15} \times H_{chim}^4 \end{aligned} \quad (52)$$

where with the temperature of the water and height of the chimney being given, the total water vapor condensation rate can be

determined at the given chimney diameter and δ. All the coefficients, Q_i, are obtained from the curve-fitting of $\dot{m}_{w-cd}^{total}$ at the given δ. Table 2 shows the obtained coefficients of Q_i at every case of δ.

Since the curve-fitting for $\dot{m}_{w-cd}^{total}$ against T_{water} and H_{chim} was carried out five times due to five different δ, each coefficient Q_i has multiple values corresponding to multiple δ. Therefore, a Q_i can be further expressed as a function of δ through curve-fitting, which gives.

$$Q_i = B_1 + B_2 \times \delta + B_3 \times \delta^2 + B_4 \times \delta^3 + B_5 \times \delta^4 \qquad (53)$$

where the coefficient B_i for equation Q_i is listed in Table 3, and the fourth-order of the polynomial equation has a sufficiently high fitting. With a given value of δ, we can find Q_i with the given coefficients B_i. When taking the determined Q_i by Eqs. (53) to Eq. (52), one can determine the water production rate.

It is important to point out that the Eqs. (52) and (53) give the total water condensation rate from the chimneys and water chambers studied in Figs. 17 and 18, where the used energy density is 600 W/m^2 and water temperature could reach 60 °C and above. These cases largely cover the operation conditions of several hours around noon time. However, at less solar heat flux and thereby less energy density used in the chamber, the water temperature can be lower than 60 °C. To meet the requirement of relative humidity of air approaching 1.0 in the chamber at temperatures lower than 60 °C and using energy less than 600 W/m^2, a large chamber diameter such as given in Fig. 16 still needs to be used. From this perspective, the chamber diameters determined in Figs. 17 and 18 are the lower limit, while the larger chamber diameters determined in Fig. 16 are the upper bound of optimal designs.

6 Conclusions and Remarks for Future Work

This paper presents a unique mathematical modeling and computation to study the coupled processes of buoyance-force-driven flow and heat/mass transfer in a solar thermal desalination system. Especially, the adoption of a thermal conductive chimney aims at making the vapor in the humid air condense more when flowing up in the chimney. The following conclusions were drawn from the modeling and simulation studies:

(1) First, the flow of air is induced due to the buoyance force and chimney effect. However, the magnitude of the buoyance force depends strongly on the heat and mass transfer from the surface of warm water to the air, which determines the temperature and humidity of the humid air that flows into the chimney. Because of the inter-dependency of flow velocities, temperatures, concentrations of vapor, and humidity of the air, an algorithm for the computational procedures to solve equations for flow, heat, and mass transfer has been developed to obtain a converged solution.
(2) A computer code was successfully developed, and computational results help us to discover various correlations between the dimensions of the water chamber and chimney with the water evaporation rate and water vapor condensation rate. Computation was conducted for a system that has been tested in our previous work. The satisfactory agreement of the simulation results with the experiment results validated the modeling and computational algorithm.
(3) For given conditions including the dimensions of the heat-dissipating chimney, the water temperature, and ambient air temperature, the simulation can find the required diameter of the water basin/chamber and the energy usage per unit area in the water basin to ensure the water temperature selected for computation is reasonable. The determination of the required diameter of the water basin is governed by a criterion that the humidity of the airflow can reach 1.0 when the airflow reaches the inlet of the chimney.
(4) The heat-dissipating chimney has a critical height that can introduce maximum airflow into a system. A chimney higher than the critical height will not help to improve the airflow but still can improve the total condensation rate of water vapor due to a large condensation heat transfer area. Optimized water chamber diameters were provided for water temperatures around 60 °C and energy usage density of 600 W/m^2, which is close to the situation of 5–6 h of operation before and after noon time in a sunny day in the summer. To cover lower energy usage density and lower water temperature operations, larger chamber diameters are needed, and values are recommended in the paper.
(5) The developed modeling and computer code provide an important tool for the design of the proposed solar–thermal desalination system for practical applications.

Finally, it is important to remark that in this study, different water temperatures were assumed to study the optimized solar collection chamber diameter and chimney height. The thereby required heat flux in the chamber was checked to not exceed 60% of the solar irradiance of 1000 W/m^2, or otherwise, dimensions are revised. The determined chamber dimensions for high water temperature and high heat flux (600 W/m^2) are the lower bound of water chamber diameter, while the larger chamber diameters determined under lower water temperature and lower available heat flux are the upper bound of the chamber diameters. Choosing an upper bound chamber diameter for a chimney, the operation can cover the conditions of various solar irradiance and still satisfy the criterion of relative humidity of 1.0 in the water chamber. Another important approach to have optimal system operation is to implement physical control of the airflow by adding a valve at the top of the chimney. Through the valve, one can also control the airflow and thus the heat and mass transfer inside the chamber, which thereby can maintain the water surface temperature being sufficiently high. While the evaporation efficiency in the system is sufficiently high due to the flow of air, the condensation of moisture in the heat-dissipating chimney still needs to be dramatically improved for more water collection. Using a higher chimney, adding a sun shield to the chimney, and heat transfer enhancement at inner and outer surface of the chimney can also be options to be studied in future work.

Acknowledgment

Grateful acknowledgment is given to the University of Arizona Office of Tech Launch WEES funding for research on Water, Environmental, and Energy Solutions (WEES). Funding supports from Consortium for Arizona-Mexico Arid Environments—CAZMEX, Salt River Project, and DOE (Grant No. DE-NA0004003) are also appreciated and gratefully acknowledged.

Conflict of Interest

There are no conflicts of interest.

Data Availability Statement

The data sets generated and supporting the findings of this article are obtainable from the corresponding author upon reasonable request.

Nomenclature

f = moody friction factor
g = gravitational acceleration (m/s^2)
k = thermal conductivity (W/°C)
r = radius location of water chamber (m)

t = thickness of chimney wall or that of cover glass of chamber (m)
u = humid air velocity inside the chimney or chamber (m/s)
x = absolute humidity ratio (kg water vapor per kg of dry air)
z = height from the inlet to up of the chimney (m)
A = area (m^2)
H = total height of chimney (m)
K = minor head loss coefficient (0.3)
M = molar mass (kg/mol)
R = gas constant (J/kg°C)
T = temperature (°C)
U = overall heat transfer coefficient ($W/m^{2\circ}C$)
V = volume flowrate of humid air in the chimney (m^3/s)
h_{air} = heat transfer coefficient of air with chamber outer surface or chimney outer surface ($W/m^{2\circ}C$)
h_{n-cham} = natural convection heat transfer coefficient outside of chamber, or
h_{n-chim} = chimney respectively ($W/m^{2\circ}C$)
$u_{average}$ = the velocity at the interface of chimney-chamber connection (m/s)
D_{chim}, $D_{chim\text{-}oD}$ = inner and outer diameter of chimney (m)
D_{cham} = diameter of chamber (m)
D_h = hydraulic diameter (m)
D_{v-air} = mass diffusivity from water vapor to air (m^2/s)
H_0 = atmospheric height $H_0 = R_{air}T_{air}/g$ (m)
T_{w-a} = the average temperature of water surface and airflow
$\tilde{h}$ = enthalpy (J/kg)
$\dot{m}$ = mass flowrate (kg/s)
$\tilde{r}$ = distance from inlet of the chamber towards center of the chamber (m)
P^{sat} = saturated water vapor pressure (Pa)
$\dot{Q}$ = energy rate, heat transfer rate (W)
$\tilde{h}_{fg}$ = latent heat of water vaporization (J/kg)
h_{chim}, h_{cham} = convection heat transfer coefficient inside chamber and chimney, respectively ($W/m^{2\circ}C$)
Cp = heat capacity (J/kg°C)
Gr = Grashof number for natural convection heat transfer
Nu = Nusselt number of heat transfer
Pr = Prandtl number for humid air
Re = Reynolds number
RH = relative humidity
Sh = Sherwood number
Sc = Schmidt number
ΔP = pressure difference or pressure loss (Pa)
δ = distance between the covering glass and the water surface (cm)
ε = depth of the potential well
κ = specific heat ratio for air
ρ = density or mass concentration (kg/m^3)
σ = collision diameter
Ω_D = collision integral

Subscripts

a, air = air
atm = atmospheric
cham = chamber
chim = chimney
conv = convective heat transfer
count = part of latent heat counted as heat loss.
cd = condensation
drive = driving force
ev = evaporation
friction = friction loss
f = saturate liquid
g = saturate vapor
in = flow inlet to a control volume
in_moistair = moist air inside chimney
loss = heat loss
minor = minor pressure loss due to change of flow duct
n-cham = natural convection-related values for chamber
n-chim = natural convection-related values for chimney
out = flow outlet of a control volume
out_dryair = dry ambient air outside of the chimney
total = total including air and water vapor
v = water vapor
va; *v-air* = water vapor versus air binary system
w, *water* = water
w-ev = water evaporation

Superscripts

cross = cross-sectional area, parameter based on cross-sectional flow area
entire-surface = a value based on the entire surface of the chamber
surface = heat or mass transfer area of a control volume
surface-in = surface area inner side
sat-vapor = saturate vapor
total = total mass, or total surface area of chamber or chimney
va = water vapor versus air
vapor = water vapor
w = water

References

[1] Elimelech, M., and Phillip, W. A., 2011, "The Future of Seawater Desalination: Energy, Technology, and the Environment," Science, **333**(6043), pp. 712–717.
[2] Kalogirou, S. A., 2005, "Seawater Desalination Using Renewable Energy Sources," Prog. Energy Combust. Sci., **31**(3), pp. 242–281.
[3] Houghton, J., 2005, "Global Warming," Rep. Prog. Phys., **68**(6), pp. 1343–1403.
[4] Li, C., Goswami, Y., and Stefanakos, E., 2013, "Solar Assisted Sea Water Desalination: A Review," Renewable Sustainable Energy Rev., **19**, pp. 136–163.
[5] Alkaisi, A., Mossad, R., and Sharifian-Barforoush, A., 2017, "A Review of the Water Desalination Systems Integrated With Renewable Energy," Energy Procedia, **110**, pp. 268–274.
[6] Zhang, Y., Sivakumar, M., Yang, S., Enever, K., and Ramezanianpour, M., 2018, "Application of Solar Energy in Water Treatment Processes: A Review," Desalination, **428**, pp. 116–145.
[7] Reif, J. H., and Alhalabi, W., 2015, "Solar-Thermal Powered Desalination: Its Significant Challenges and Potential," Renewable Sustainable Energy Rev., **48**, pp. 152–165.
[8] Sharon, H., and Reddy, K., 2015, "A Review of Solar Energy Driven Desalination Technologies," Renewable Sustainable Energy Rev., **41**, pp. 1080–1118.
[9] Ghaffour, N., Bundschuh, J., Mahmoudi, H., and Goosen, M. F., 2015, "Renewable Energy-Driven Desalination Technologies: A Comprehensive Review on Challenges and Potential Applications of Integrated Systems," Desalination, **356**, pp. 94–114.
[10] Sayyaadi, H., and Saffari, A., 2010, "Thermoeconomic Optimization of Multi Effect Distillation Desalination Systems," Appl. Energy, **87**(4), pp. 1122–1133.
[11] Palenzuela, P., Alarcón, D., Zaragoza, G., Blanco, J., and Ibarra, M., 2013, "Parametric Equations for the Variables of a Steady-State Model of a Multi-Effect Desalination Plant," Desalin. Water Treat., **51**(4–6), pp. 1229–1241.
[12] Hosseini, S. R., Amidpour, M., and Behbahaninia, A., 2011, "Thermoeconomic Analysis With Reliability Consideration of a Combined Power and Multi Stage Flash Desalination Plant," Desalination, **278**(1–3), pp. 424–433.
[13] Cohen-Tanugi, D., Lin, L.-C., and Grossman, J. C., 2016, "Multilayer Nanoporous Graphene Membranes for Water Desalination," Nano Lett., **16**(2), pp. 1027–1033.
[14] Anvari, A., Azimi Yancheshme, A., Kekre, K. M., and Ronen, A., 2020, "State-of-the-Art Methods for Overcoming Temperature Polarization in Membrane Distillation Process: A Review," J. Membr. Sci., **616**, p. 118413.
[15] Shalaby, S., 2017, "Reverse Osmosis Desalination Powered by Photovoltaic and Solar Rankine Cycle Power Systems: A Review," Renewable Sustainable Energy Rev., **73**, pp. 789–797.
[16] Das, R., Ali, M. E., Abd Hamid, S. B., Ramakrishna, S., and Chowdhury, Z. Z., 2014, "Carbon Nanotube Membranes for Water Purification: A Bright Future in Water Desalination," Desalination, **336**, pp. 97–109.
[17] Dong, H., Zhao, L., Zhang, L., Chen, H., Gao, C., and Winston Ho, W. S., 2015, "High-Flux Reverse Osmosis Membranes Incorporated With NaY Zeolite Nanoparticles for Brackish Water Desalination," J. Membr. Sci., **476**, pp. 373–383.

[18] Al-Amshawee, S., Yunus, M. Y. B. M., Azoddein, A. A. M., Hassell, D. G., Dakhil, I. H., and Hasan, H. A., 2020, "Electrodialysis Desalination for Water and Wastewater: A Review," Chem. Eng. J., **380**, p. 122231.
[19] Mettawee, E.-B. S., and Assassa, G. M., 2006, "Experimental Study of a Compact PCM Solar Collector," Energy, **31**(14), pp. 2958–2968.
[20] Zhao, D., Li, Y., Dai, Y., and Wang, R., 2011, "Optimal Study of a Solar Air Heating System With Pebble bed Energy Storage," Energy Convers. Manage., **52**(6), pp. 2392–2400.
[21] Nayi, K. H., and Modi, K. V., 2018, "Pyramid Solar Still: A Comprehensive Review," Renewable Sustainable Energy Rev., **81**, pp. 136–148.
[22] Fathy, M., Hassan, H., and Salem Ahmed, M., 2018, "Experimental Study on the Effect of Coupling Parabolic Trough Collector With Double Slope Solar Still on Its Performance," Sol. Energy, **164**, pp. 54–61.
[23] Sathyamurthy, R., El-Agouz, S. A., Nagarajan, P. K., Subramani, J., Arunkumar, T., Mageshbabu, D., Madhu, B., Bharathwaaj, T., and Prakash, N., 2017, "A Review of Integrating Solar Collectors to Solar Still," Renewable Sustainable Energy Rev., **77**, pp. 1069–1097.
[24] Tiwari, G., Dimri, V., and Chel, A., 2009, "Parametric Study of an Active and Passive Solar Distillation System: Energy and Exergy Analysis," Desalination, **242**(1–3), pp. 1–18.
[25] Sampathkumar, K., Arjunan, T., Pitchandi, P., and Senthilkumar, P., 2010, "Active Solar Distillation—A Detailed Review," Renewable Sustainable Energy Rev., **14**(6), pp. 1503–1526.
[26] Haaf, W., Friedrich, K., Mayr, G., and Schlaich, J., 1983, "Solar Chimneys Part I: Principle and Construction of the Pilot Plant in Manzanares," Int. J. Solar Energy, **2**(1), pp. 3–20.
[27] Haaf, W., 1984, "Solar Chimneys: Part ii: Preliminary Test Results From the Manzanares Pilot Plant," Int. J. Sustainable Energy, **2**(2), pp. 141–161.
[28] Zuo, L., Zheng, Y., Li, Z., and Sha, Y., 2011, "Solar Chimneys Integrated With Sea Water Desalination," Desalination, **276**(1–3), pp. 207–213.
[29] Zuo, L., Yuan, Y., Li, Z., and Zheng, Y., 2012, "Experimental Research on Solar Chimneys Integrated With Seawater Desalination Under Practical Weather Condition," Desalination, **298**, pp. 22–33.
[30] Zuo, L., Ding, L., Chen, J., Liu, Z., Qu, N., Zhou, X., and Yuan, Y., 2018, "The Effect of Different Structural Parameters on Wind Supercharged Solar Chimney Power Plant Combined With Seawater Desalination," Energy Convers. Manage., **176**, pp. 372–383.
[31] Zuo, L., Liu, Z., Zhou, X., Ding, L., Chen, J., Qu, N., and Yuan, Y., 2019, "Preliminary Study of Wind Supercharging Solar Chimney Power Plant Combined with Seawater Desalination by Indirect Condensation Freshwater Production," Desalination, **455**, pp. 79–88.
[32] Zhou, X., Xiao, B., Liu, W., Guo, X., Yang, J., and Fan, J., 2010, "Comparison of Classical Solar Chimney Power System and Combined Solar Chimney System for Power Generation and Seawater Desalination," Desalination, **250**(1), pp. 249–256.
[33] Asayesh, M., Kasaeian, A., and Ataei, A., 2017, "Optimization of a Combined Solar Chimney for Desalination and Power Generation," Energy Convers. Manage., **150**, pp. 72–80.
[34] Ming, T., Gong, T., de Richter, R. K., Liu, W., and Koonsrisuk, A., 2016, "Freshwater Generation From a Solar Chimney Power Plant," Energy Convers. Manage., **113**, pp. 189–200.
[35] Ming, T., Gong, T., de Richter, R. K., Cai, C., and Sherif, S., 2017, "Numerical Analysis of Seawater Desalination Based on a Solar Chimney Power Plant," Appl. Energy, **208**, pp. 1258–1273.
[36] Ming, T., Gong, T., de Richter, R. K., Wu, Y., and Liu, W., 2017, "A Moist air Condensing Device for Sustainable Energy Production and Water Generation," Energy Convers. Manage., **138**, pp. 638–650.
[37] Bonnelle, D., 2004, "Solar Tower, Water Spraying Energy Tower, and Linked Renewable Energy Conversion Devices: Presentation, Critics and Proposals; Tour Solaire, Tour a Vaporisation D'eau, et Modes de Conversion D'energie Renouvelable: Presentation, Critiques et Suggestions. https://www.osti.gov/etdeweb/biblio/20613580
[38] Krätzig, W. B., 2013, "Physics, Computer Simulation and Optimization of Thermo-Fluid Mechanical Processes of Solar Updraft Power Plants," Sol. Energy, **98**, pp. 2–11.
[39] Von Backström, T. W., Harte, R., Hoffer, R., Kratzig, W. B., Kroger, D. G., Niemann, H.-J., and Van Zijl, G. P. A. G., 2008, "State and Recent Advances in Research and Design of Solar Chimney Power Plant Technology," VGB Power Tech, **88**(7), pp. 64–71.
[40] Zhai, Y., Ma, Y., David, S. N., Zhao, D., Lou, R., Tan, G., Yang, R., and Yin, X., 2017, "Scalable-Manufactured Randomized Glass-Polymer Hybrid Metamaterial for Daytime Radiative Cooling," Science, **355**(6329), pp. 1062–1066.
[41] Hu, Q., 2019, "Studies of Flow and Heat/Mass Transfer in Water Desalination Tower," Master thesis, University of Arizona, Tucson, AZ. https://www.proquest.com/pagepdf/2305531143?accountid=8360
[42] Hu, Q., Wang, X., Gamil, A., and Li, P., 2023, "Experimental Study of Desalination Using a System Integrated by a Glass-Covered Solar Collection Water Basin and a Heat Dissipating Chimney," Energy Nexus, **9**, p. 100171.
[43] Schlaich, J., 1995, *The Solar Chimney: Electricity From the Sun*, Edition Axel Menges, Stuttgart.
[44] dos S. Bernardes, M. A, Voß, A., and Weinrebe, G., 2003, "Thermal and Technical Analyses of Solar Chimneys," Sol. Energy, **75**(6), pp. 511–524.
[45] Lienhard IV, J. H., and Lienhard V, J. H., 2005, *A Heat Transfer Textbook*, Phlogiston Press, Cambridge, MA.
[46] Bergman, T., Lavine, A., Incropera, F., and DeWitt, D., 2019, *Fundamentals of Heat and Mass Transfer*, 8th ed., Wiley, New York.
[47] Lloyd, J., and Moran, W., 1974, "Natural Convection Adjacent to Horizontal Surface of Various Planforms," ASME J. Heat Transfer, **96**(4), pp. 443–447.
[48] Elhammeli, A. A., Muntasser, M. A., Lindblom, J., and Nordell, B., 2017, "Producing Water by Condensation of Humid air in Buried Pipe," Proceedings of 7th Annual Conference on Industrial Engineering and Operations Management, Rabat, Morocco, Apr. 11–13, IEOM Society, pp. 2270–2281.
[49] Yang, S., and Zhang, Z., 1994, "An Experimental Study of Natural Convection Heat Transfer From a Horizontal Cylinder in High Rayleigh Number Laminar and Turbulent Regions," Institution of Chemical Engineers Symposium Series, Brighton, UK, Aug. 14–18, Vol. 135, Hemisphere Publishing Corporation, pp. 185–185.
[50] Tsilingiris, P., 2008, "Thermophysical and Transport Properties of Humid Air at Temperature Range Between 0 and 100 C," Energy Convers. Manage., **49**(5), pp. 1098–1110.
[51] Moran, M., Shapiro, H., Boettner, D., and Bailey, M., 2018, *Fundamentals of Engineering Thermodynamics*, 9th ed., Wiley, New York.
[52] Wilke, C., 1950, "A Viscosity Equation for Gas Mixtures," J. Chem. Phys., **18**(4), pp. 517–519.
[53] Reid, R. C., Prausnitz, J. M., and Poling, B. E., 1987, *The Properties of Gases and Liquids*, McGraw-Hill, New York.
[54] Morvay, Z., and Gvozdenac, D., 2008, *Applied Industrial Energy and Environmental Management*, John Wiley & Sons, New York.
[55] Mason, E., and Saxena, S., 1958, "Approximate Formula for the Thermal Conductivity of Gas Mixtures," Phys. Fluids, **1**(5), pp. 361–369.